Arch. Mech., 43, 2–3, pp. 399—435, Warszawa 1991

Constitutive modelling of spall fracture(*)

J. EFTIS and J.A. NEMES (WASHINGTON, D.C.)

A PHENOMENOLOGICAL viscoplastic constitutive theory that includes the material microvoid volume fraction as a scalar-valued damage variable has recently been used to model high strain-rate deformation and ductile spall fracture caused by high velocity plate impact. Numerical calculations that simulate three experimental plate-impact configurations give realistic results, demonstrating the theory's ability to describe ductile spall phenomena. An oxygen-free high purity copper material was assumed for the plate material. The numerical simulations describe the normal and oblique impact of plates having equal lateral dimensions, and the normal impact of a small circular flyer plate with a larger diameter circular target plate. For the plate configurations with large lateral dimensions stress wave profiles are calculated, as are target rear-surface velocity-time profiles and damage distributions across the target thickness. For the circular plate impact the distribution of damage within the target, the target plate configurations at spall and at post-spall, including fragmentation of the target, are calculated. In the only comparisons with experiment that could be made, the predicted stress and velocity-time profiles and the damage distribution for the non-oblique impact compares well with available experimental data for OFHC copper.

Fenomenologiczna teoria konstytutywna lepkoplastyczności uwzględniająca objętościowy udział mikropustek w materiale jako skalarną zmienną uszkodzenia została ostatnio wykorzystana do opisu dużych prędkości deformacji i ciągliwego dynamicznego zniszczenia spowodowanego uderzeniem z dużą prędkością. Numeryczne obliczenia, które stanowią symulację trzech doświadczalnych układów zderzających się płyt dają zadowalające rezultaty, co wskazuje na przydatność teorii do opisu zjawisk dynamicznego zniszczenia. Jako materiał badanej płyty przyjęto wolną od tlenu wysokiej czystości miedź. Numeryczne symulacje opisują ortogonalne i ukośne zderzenie płyt mających jednakowy wymiar podłużny oraz ortogonalne zderzenie mniejszej poruszającej się płyty kołowej z kołową płytą tarczy o większej średnicy. Dla konfiguracji płyt z dużym wymiarem podłużnym określono profil fali naprężenia, jak również zmianę prędkości tylnej powierzchni płyty-tarczy w funkcji czasu oraz rozkład uszkodzenia po grubości tarczy. W przypadku zderzenia płyt kołowych określono rozkład uszkodzeń w tarczy, konfiguracje płyty-tarczy w chwili zniszczenia i po zniszczeniu z uwzględnieniem fragmentacji. Możliwe do przeprowadzenia porównania z rezultatami eksperymentalnymi przewidywanych naprężeń, zmian prędkości w czasie oraz rozkładu uszkodzeń dla ortogonalnego zderzenia dają zgodne wyniki w przypadku miedzi OFHC.

Феноменологическая определяющая теория вязкопластичности, учитывающая объемное участие микропустот в материале как скалярную переменную повреждения, в последнее время использована для описания больших скоростей деформаций и тягучего динамического разрушения, вызванного ударом с большой скоростью. Численные расчеты, которые составляют имитацию трех экспериментальных систем сталкивающихся плит, дают удовлетворяющие результаты, что показывает на пригодность теории для описания явлений динамического разрушения. Как материал исследуемой плиты принята, свободная от кислорода, медь высокой чистоты. Численные имитации описывают ортогональные и косые столкновения плит, имеющих одинаковый продольный размер, а также ортогональное столкновение меньшей, движущейся круговой плиты

(*) An expanded version of an invited lecture-paper at the 28th Polish Solid Mechanics Conference, Kozubnik, Poland, Sept. 4—8, 1990.

с круговой плитой-мишенью с большим диаметром. Для конфигурации плит с большим продольным размером определен профиль волны напряжения, как тоже изменение скорости задней поверхности плиты-мишени в функции времени и распределения повреждения по толщине мишени. В сличае столкновения круговых плит определено распределение повреждений в мишени, конфигурации плиты-мишени в момент разрушения и после разрушения, с учетом фрагментации. Возможные дла проведения сравнения с экспериментальными результатами предсказываемых напряжений, изменений скорости во времени и распределения повреждений для ортогонального столкновения дают совпадающие результаты в случае меди OFHC.

1. Introduction

SPALL FRACTURE (spallation) is a particular kind of fracture that results from the tension produced by the interaction of propagating rarefaction waves. Such waves can be caused by the impact of a projectile against a target [1], the detonation of a high explosive in direct contact with the target [2], or by sudden deposition of an intense pulse of energy on the target surface [3]. More specifically, in the case of plate impact the initial compressive stress wave travelling across the target plate reflects back at the free surface as a propagating tensile wave. A similar process, oppositely directed, occurs in the flyer plate. The superposition of the propagating tensile wave fronts, if of sufficient intensity (amplitude) and time duration, can cause partial or complete separation of the material along a plane perpendicular to the direction of the wave fronts (cf. Fig. 1, [4–6]). Spallation as a particular manifestation of

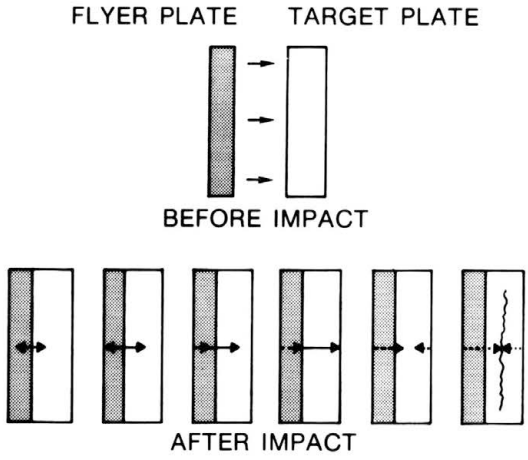

FIG. 1. Schematic of spall fracture induced by plate impact.

dynamic fracture and fragmentation in general, has been the subject of much recent interest, particularly at the Stanford Research Institute [7–13], and the Sandia National Laboratories [14–18]. The review articles on spall and dynamic fracture by MEYERS and AIMONE [19], and by CURRAN, SEAMAN

and SHOCKEY [20], provide access to much of the extensive literature on the subject.

A plate-impact-spall experiment consists essentially of a thin flyer plate acting as a high speed projectile that strikes a target plate with an impact velocity that usually ranges between 100—400 m/s. The transit time of the stress waves that propagate across the plates is of the order of $10^{-7} - 10^{-6}$ s, causing very high strain rates that range between $10^4 - 10^6$ s^{-1}, and deformation that is essentially adiabatic. The impact produces mean stresses that can vary in the 5—50 kbar low to moderate shock stress range.

In describing mechanical behavior of polycrystalline materials for ordinary engineering applications, the presence of very small voids within the polycrystal structure is not significant. However, in circumstances where material degradation occurs, either because of high intensity stress loading, or because of advanced deformation, the porosity of the material becomes important in attempting to describe its mechanical response. Microvoids in polycrystalline metals can range in size from $10^{-2} - 10^{-5}$ cm., with an average density of the order of 10^6 per cm^3, and an average initial void volume fraction between $10^{-3} - 10^{-4}$.

Post-fracture photo-micrographic observations have shown that spallation represents the end result of an accumulation of microdamage that takes place during the tensile phase of the stress wave loading. Figure 2 provides an illustration of microdamage that consists of somewhat disoriented microcracks of different sizes to the left, and of voids of varying size and configuration to the right. In ductile materials the microdamage consists mostly of microvoids that nucleate, grow and finally coalesce to form the plane of separation within the material body (cf. [20]). In keeping with these known physical features of ductile spallation, PERZYNA [21] has recently formulated a rate-type visco-plastic-damage constitutive theory that includes the microvoid volume fraction of the polycrystalline material as a scalar internal variable, which is regarded as a damage measure that serves to quantify ductile type material degradation. A local fracture criterion is utilized based upon attainment of a critical void volume fraction. The constitutive model in the form shown here assumes no temperature change or heat conduction, and is appropriate therefore to situations of moderate shock where the temperature changes induced by the high strain rate deformation are not significant.

The constitutive theory has recently been utilized in an attempt to describe the spall fracture of thin plate for three different plate-impact geometries [21–29]. For the first, plates that have equal lateral dimension and unequal thickness, collide with the direction of the velocity of the flyer plate normal to the plane of the plates (cf. Fig. 1). For this configuration the spall process takes place under conditions of uniaxial strain along the direction of the plate thickness. In the second configuration the impact of the parallel plates occurs

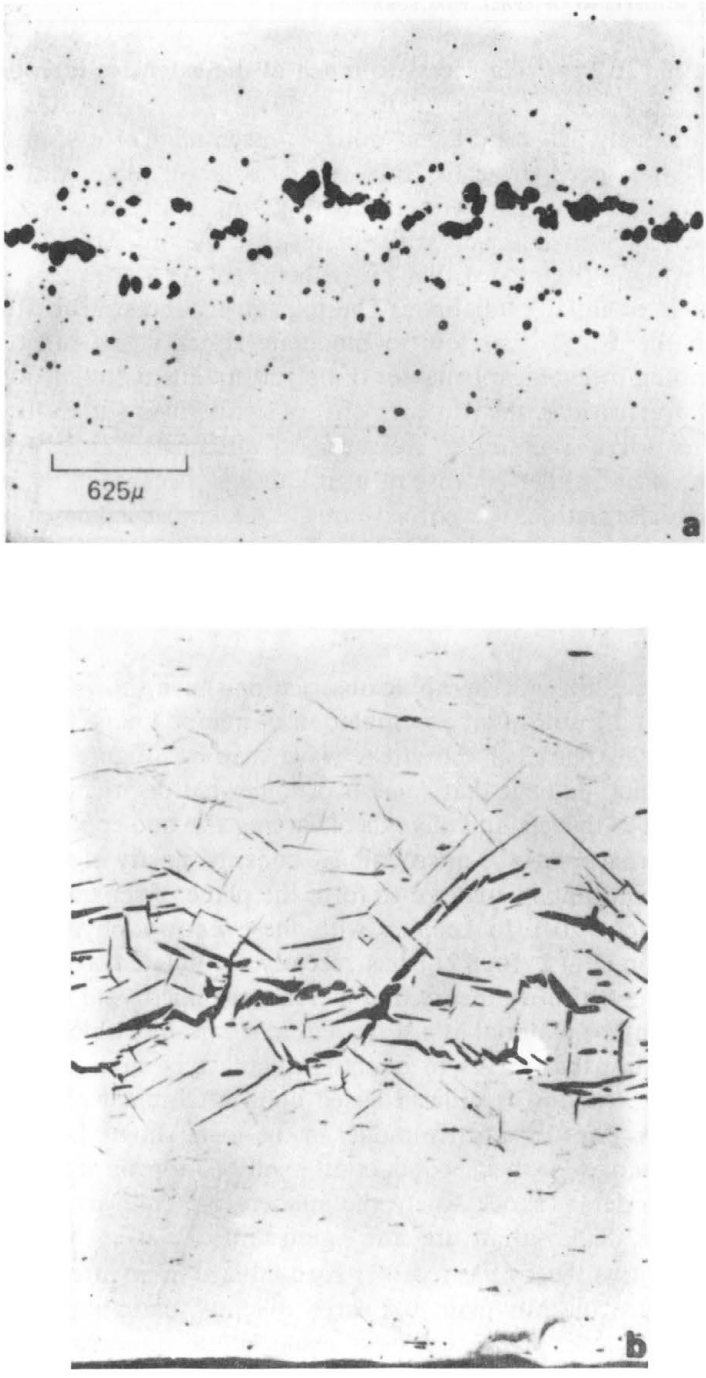

FIG. 2. Photo-micrograph of microdamage caused by impact.

along the direction inclined relative to the flyer velocity direction, i.e., oblique impact. This results in propagating waves of combined pressure and shear, with corresponding normal and shear strains in the direction of the plate thickness. This configuration is shown in Fig. 15. The third configuration involves non-oblique impact of parallel circular plates having different diameters and thicknesses. The circular plate configuration, shown in Fig. 23, provides a more complex situation of multi-dimensional axisymmetric strains. Because of the edge effect of the smaller flyer plate, nonplanar as well as planar waves are generated and the region of spall covers only part of the target plate diameter, resulting possibly in partial spall, or spall with post-spall fragmentation.

2. Elastic-viscoplastic solid with microvoids

2.1. Constitutive equations

The polycrystalline medium is assumed to be permeated with micro-voids, where $\xi = \xi(\mathbf{x}, t)$ represents the void volume fraction $\xi = (V - V^s)/V$ at location $\mathbf{x}$ and time t, V is the volume of a material microelement and V^s is the solid constituent. The average initial void volume fraction for polycrystalline metals is usually of the order $\xi_0 = 0.001 - 0.0001$, which for the more usual kinds of engineering calculations is assumed to be negligible.

The constitutive equations are expressed in rate form where the rate of deformation tensor is assumed to have additive elastic and plastic components

$$\mathbf{D} = \mathbf{D}^e + \mathbf{D}^p. \tag{2.1}$$

The elastic deformation is of small order in strain, allowing the rate of elastic deformation to be expressed as a linear function of the stress rate

$$\mathbf{D}^e = \frac{1}{2\bar{\mu}}\left[\overset{\nabla}{\mathbf{T}} - \frac{\bar{\nu}}{1+\bar{\nu}}\left(\mathrm{tr}\overset{\nabla}{\mathbf{T}}\right)\mathbf{1}\right], \tag{2.2}$$

where $\overset{\nabla}{\mathbf{T}}$ represents an objective stress-rate of the Cauchy stress tensor $\mathbf{T}$. The elastic properties of the solid are altered as the void volume fraction of the material changes. According to the hollow sphere model proposed by MACKENZIE [30], the elastic shear and bulk moduli can be expressed in relation to their values for the ideal solid (without microvoids) through the relations

$$\bar{\mu} = \mu(1-\xi)\left(1 - \frac{6K+12\mu}{9K+8\mu}\xi\right), \tag{2.3}$$

$$\bar{K} = \frac{4\mu K(1-\xi)}{4\mu + 3K\xi} \tag{2.4}$$

and

$$\bar{\nu} = \frac{1}{2}\,\frac{3\bar{K} - 2\bar{\mu}}{3\bar{K} + \bar{\mu}}, \tag{2.5}$$

where μ, K are the elastic shear and bulk moduli values for the ideal material.

The inelastic rate at which the microvoid permeated material deforms can be described by the following set of relations [31, 21],

$$\begin{aligned} \mathbf{D}^p &= \frac{\gamma}{\phi}\,\Phi(\hat{F})\frac{\partial f}{\partial \mathbf{T}} \quad \text{for} \quad \hat{F} > 0, \\ \mathbf{D}^p &= 0 \qquad\qquad\quad \text{for} \quad \hat{F} \leqslant 0. \end{aligned} \tag{2.6}$$

Here Φ is a material functional of the yield function

$$\hat{F} = \frac{f}{\varkappa} - 1, \tag{2.7}$$

while ϕ serves as a rate of deformation control function that has as its argument the ratio $[(I_2/I_2^s) - 1]$. It is defined such that for $I_2 = I_2^s$, $\phi(0) = 0$ and for $I_2 < I_2^s$, $\phi(...) \equiv 0$. The rate of deformation invariant

$$I_2 = \left\| (\Pi_{\mathbf{D}'})^{\frac{1}{2}} \right\| \tag{2.8}$$

with $\|(...)\|$ denoting absolute value, and

$$\Pi_{\mathbf{D}'} = \frac{1}{2}\left[- \operatorname{tr}(\mathbf{D}' \cdot \mathbf{D}')\right], \tag{2.9}$$

$$\mathbf{D}' = \mathbf{D} - \frac{1}{2}(\operatorname{tr}\mathbf{D})\mathbf{1}. \tag{2.10}$$

The value $I_2 = I_2^s$ signifies the quasi-static rate of deformation, that is, the strain rate below which no significant rate effect of the viscoplastic material is observed by the usual means of laboratory testing at the temperature of interest. The constant

$$\gamma = \frac{\gamma_0}{\varkappa_0} \tag{2.11}$$

includes the material viscosity coefficient γ_0 and the rate-independent yield stress $\varkappa_0 = (1/\sqrt{3})\,T_y$.

The presence of microvoids introduces compressibility into the otherwise incompressible plastic deformation. Therefore the yield function f, in reflecting this circumstance includes the first invariant of the stress, [32–34],

$$f = f(J_1, J_2', \xi) = J_2' + n\xi J_1^2, \tag{2.12}$$

where

$$J_1 = I_{\mathbf{T}} = \operatorname{tr}\mathbf{T}, \tag{2.13}$$

$$J_2' = -\Pi_{\mathbf{T}'} = \frac{1}{2}\operatorname{tr}(\mathbf{T}'\cdot\mathbf{T}'), \tag{2.14}$$

$$\mathbf{T}' = \mathbf{T} - \frac{1}{2}(\operatorname{tr}\mathbf{T})\mathbf{1}. \tag{2.15}$$

The material coefficient n proportions the relative effect of the dilatational and deviatoric contributions to the yield. The isotropic hardening of the material and the concomitant material softening as the microvoid volume fraction increases, is expressed through the yield function

$$\varkappa = \varkappa(\varepsilon^p, \xi) = [q + (\varkappa_0 - q)e^{-\beta\varepsilon^p}]^2\left[1 - n_1\xi^{1/2}\right]^2. \tag{2.16}$$

The coefficients q, β are material hardening parameters, e.g., q is the stress at which the strain hardening saturates. The material parameter n_1 is identified below, and ε^p is the equivalent plastic strain invariant

$$\varepsilon^p = \int_0^t \frac{2}{\sqrt{3}}\left\|(\Pi_{\mathbf{D}^p})^{1/2}\right\| dt'. \tag{2.17}$$

It should be noted that the form for the isotropic hardening appearing in Eq. (2.16), which assumes nonlinear strain hardening that saturates as the strain progresses, is a modification of the linear strain hardening proposed by PERZYNA [21]. The reader is directed to Ref. [22] for discussion of the reasons requiring such a change.

The material functional and the rate of deformation control function are assumed to be power functions of their arguments

$$\Phi(\hat{F}) = \left(\frac{f(J_1, J_2', \xi)}{\varkappa(\varepsilon^p, \xi)} - 1\right)^{m_1}, \quad \phi\left(\frac{I_2}{I_2^s} - 1\right) = \left(\frac{I_2}{I_2^s} - 1\right)^m \tag{2.18}$$

with m_1, m as material parameters. The general form Eq. (2.6) for the viscoplastic rate of deformation can now be given explicitly as

$$\mathbf{D}^p = \frac{\gamma_0}{\left(\frac{I_2}{I_2^s} - 1\right)^m}\left[\frac{J_2' + n\xi J_1^2}{[q + (\varkappa_0 - q)\, e^{-\beta\varepsilon^p}]^2[1 - n_1\xi^{1/2}]^2} - 1\right]^{m_1} \times \frac{1}{\varkappa_0}(2n\xi J_1 \mathbf{1} + \mathbf{T}'). \tag{2.19}$$

From Eq. (2.7)

$$\Phi(\hat{F}) = \frac{1}{\gamma}\{\mathrm{tr}(\mathbf{D}^p \cdot \mathbf{D}^p)\}^{1/2}\phi\left\{\mathrm{tr}\left(\frac{\partial f}{\partial \mathbf{T}} \cdot \frac{\partial f}{\partial \mathbf{T}}\right)\right\}^{-1/2}, \tag{2.20}$$

which together with Eqs. (2.11), (2.12), (2.16) and (2.18) produces the revealing relation

$$f = J_2' + n\xi J_1^2 = [q + (\varkappa_0 - q)e^{-\beta\varepsilon^p}]^2[1 - n_1\xi^{1/2}]^2 \times \left\{1 + \left[\frac{(\mathrm{tr}(\mathbf{D}^p \cdot \mathbf{D}^p)\}^{1/2}}{\gamma_0}\left(\frac{I_2}{I_2^s} - 1\right)^m \varkappa_0 (12n^2\xi^2 J_1^2 + 2J_2')^{-1/2}\right]^{1/m_1}\right\}, \tag{2.21}$$

which describes the continuous change of the plastic flow stress as a result of isotropic hardening, the strain-rate sensitivity of the inelastic deformation, and the material softening associated with growth of the microvoid volume fraction. Equation (2.21) is very useful for determining the values of the material parameters.

2.2. Evolution equation for the void volume fraction

The material degradation or damage is represented by increase of the void volume fraction from its average initial value ξ_0. At nonelevated temperature and high rates of deformation microvoids increase due to diffusional micro-processes is not significant. Therefore nucleation of new voids and volume growth represent the essential micromechanisms that are operative for ductile spall damage at ordinary temperatures.

At the high rates of strain associated with deformation caused by high velocity impact, the thermally activated mechanism for microvoid nucleation is considered the most important. It can be modeled by the form suggested by SEAMAN *et al.* [9, 20], which subsequently was modified by PERZYNA [21] to futher include the effects of void interaction,

$$\left(\frac{d\xi}{dt}\right)_n = \frac{h(\xi)}{1 - \xi}\left[\exp\left(\frac{m_2|\sigma - \sigma_N|}{k0}\right) - 1\right], \tag{2.22}$$

where $m_2|\sigma - \sigma_N|/k0$ is the nucleation activation energy, $\sigma = (1/3)J_1$ is the mean stress, σ_n is the threshold mean stress for nucleation, 0 is the

temperature, k is the Boltzmann constant, and m_2 is a material parameter. The material function $h(\xi)$ is meant to account for the effects of void interaction on void nucleation.

The calculation for the rate of increase of the volume fraction of the microvoids uses the hollow sphere model where the voids of the solid are replaced by a random distribution of spherical voids of arbitrary size embedded in a viscoplastic material that strain-hardens nonlinearly, (cf. Fig. 3), and is given by the set of relations [25]

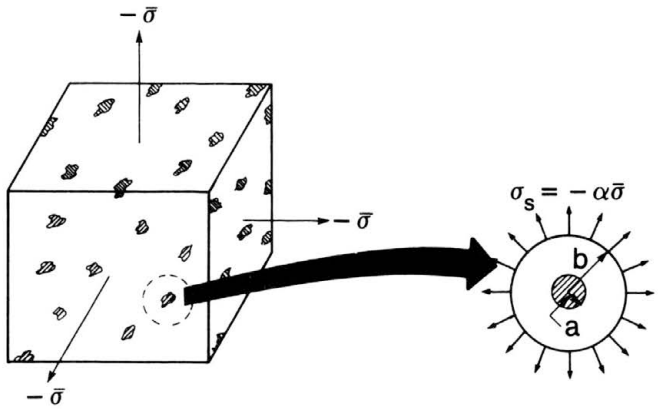

FIG. 3. Element of the solid with microvoids replaced by idealized spherical voids.

$$\left(\frac{d\xi}{dt}\right)_g = \frac{1}{\eta} g(\xi) F(\xi, \xi_0) (\sigma - \sigma_G), \tag{2.23}$$

for $\sigma < \sigma_G$ (tensile stress is taken as negative), where

$$F(\xi, \xi_0) = \frac{\sqrt{3}}{2} \xi \left(\frac{1-\xi}{1-\xi_0}\right)^{\frac{2}{3}} \left[\xi - \left(\frac{\xi}{\xi_0}\right)^{\frac{2}{3}}\right]^{-1}, \tag{2.24}$$

$$\sigma_G = \frac{1}{\sqrt{3}} (1-\xi) \ln\left(\frac{1}{\xi}\right) [2q + (\varkappa_0 - q) F_1(\xi, \xi_0)] \tag{2.25}$$

and

$$F_1(\xi, \xi_0) = \exp\left[\frac{2}{3}\beta \frac{(\xi_0 - \xi)}{\xi(1-\xi_0)} \left(\frac{1-\xi}{1-\xi_0}\right)^{-\frac{2}{3}} \left(\frac{\xi_0}{\xi}\right)^{-\frac{2}{3}}\right] + \exp\left[\frac{2}{3}\beta \frac{(\xi_0 - \xi)}{(1-\xi_0)} \left(\frac{1-\xi}{1-\xi_0}\right)^{-\frac{2}{3}}\right]. \tag{2.26}$$

This result generalizes the earlier calculations of CARROLL and HOLT [35], JOHNSON [36] and PERZYNA [21]. In these expressions σ_G represents the void growth threshold stress, η is the microviscosity parameter (associated with the microvoid growth), and $g(\xi)$ is a material function that accounts for the effects of void interaction during microvoid growth. Since the functions $h(\xi)$ and $g(\xi)$ serve to hasten void nucleation and growth rates, they can be associated with the void coalescence that takes place at the terminal stage of the microvoid growth process. On the basis of observed void volume distributions in spalled plates the material function $g(\xi)$ was chosen to have the exponential form $g(\xi) = e^{\alpha\xi}$, where α is a material parameter, while the function $h(\xi)$ was assumed to have a constant value (cf. Ref. [37, 20]).

Thus for the given circumstances the instantaneous value of the void volume fraction $\xi(\mathbf{x}, t)$ appearing in the constitutive relations (2.3), (2.4), (2.19) and (2.21) can be determined by time integration of the void fraction rate equation

$$\frac{d\xi}{dt} = \frac{\partial \xi}{\partial t} + \mathbf{v}\cdot\operatorname{grad}(\xi) = \frac{h(\xi)}{1-\xi}\left[\exp\left(\frac{m_2|\sigma - \sigma_N|}{k\theta}\right) - 1\right] + \frac{1}{\eta} g(\xi) F(\xi, \xi_0)(\sigma - \sigma_G). \tag{2.27}$$

2.3. Local criteria for ductile fracture

Micrographs taken from cross-sections of spalled plates show quite clearly that ductile spallation represents, essentially, the macroscopic terminal stage of the microvoid growth process [10, 20]. Accordingly, local criteria for ductile fracture can be defined as the attainment of a critical void volume fraction, that is, $\xi = \xi_F$, at which the material element (point) of the body experiences separation with corresponding catastrophic increase of the rate of inelastic deformation. Thus

$$\lim_{\xi \to \xi_F} \mathbf{D}^p \to \infty, \tag{2.28}$$

whereby from Eqs. (2.19) and (2.16) it follows that

$$\varkappa(\varepsilon^p, \xi)_{\xi=\xi_F} = [q + (\varkappa_0 - q)\, e^{-\beta\varepsilon^p}]^2\, [1 - n_1\, \xi_F^{\frac{1}{3}}]^2 = 0, \tag{2.29}$$

identifying the material parameter n_1

$$n_1 = \frac{1}{(\xi_F)^{\frac{1}{3}}}. \tag{2.30}$$

2.4. Values for the material parameters

In the results subsequently described and discussed, oxygen-free high purity copper was assumed for the plate material because of the experimental data from high strain-rate tests, and from spall fracture studies, that is available in the literature. Discussion of the evaluation and assignment of the material parameter values and the material functions for OFHC copper can be found in Refs. [22, 23, 37]. Consequently only a tabulated summary is provided by Table 1.

Table 1. OFHC copper material parameters.

$\mu = 4.84 \times 10^4$ MPa	$n = 0.25$
$K = 14.0 \times 10^4$ MPa	$\xi_0 = 3 \times 10^{-4}$
$q = 125$ MPa	$\xi_F = 0.32$
$\beta = 6.14$	$n_1 = 1.77$
$\rho_R = 8.93$ gm/cm^3	$\sigma_N = 500$ MPa (tension)
$I_2^* = 7 \times 10^{-4}$ s^{-1}	$m_2 = 2.025 \times 10^{-23}$ cm^3
$\varkappa_0 = 9.31$ MPa	$h = 70.37$
$\gamma_0 = 337$ s^{-1}	$\alpha = 20$
$m = 1/2$	$k\theta = 4.05 \times 10^{-21}$ J
$m_1 = 2$	$\eta = 120$ Poise

2.5. Predicted stress-strain-damage material response

The capability of the constitutive theory to model the rate sensitivity and hardening characteristics of polycrystalline material response, as well as the damaging effects associated with increase of the microvoid volume fraction are shown by Figures 4—6. The uniaxial stress-strain and the uniaxial strain-stress relations, shown graphically by these figures, are obtained by specializing the set of constitutive relations given in Sect. 2.2 using the material parameters listed in Table 1 (cf. Ref. [22]).

The predicted curves of Figures 4 and 5 assume no microvoid volume increase. The first set illustrate the sensitivity of the yield stress to strain rate, particularly at the higher rates, qualitatively similar to the experimental data for copper reported by NICHOLAS [38], and DOWLING *et al.* [39]. The predicted stress-uniaxial strain response for OFHC copper at different strain rates shown by Fig. 5, are qualitatively similar in general features to the experimentally constructed stress-uniaxial strain curves for aluminum 1060 reported by KARNES [40]. They also demonstrate the yield stress (Hugoniot elastic limit) sensitivity of copper to high rates of strain. Both sets of figures show the relative softness of copper at moderate strain rates.

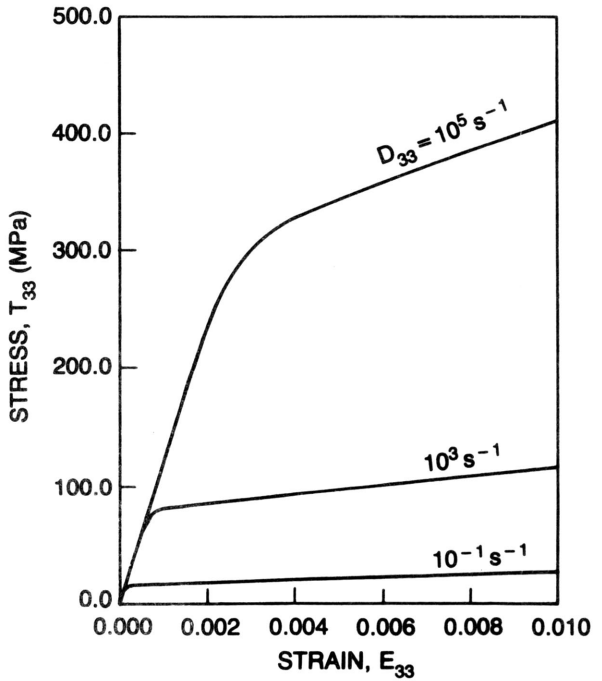

FIG. 4. Predicted uniaxial stress-strain response at different strain rates.

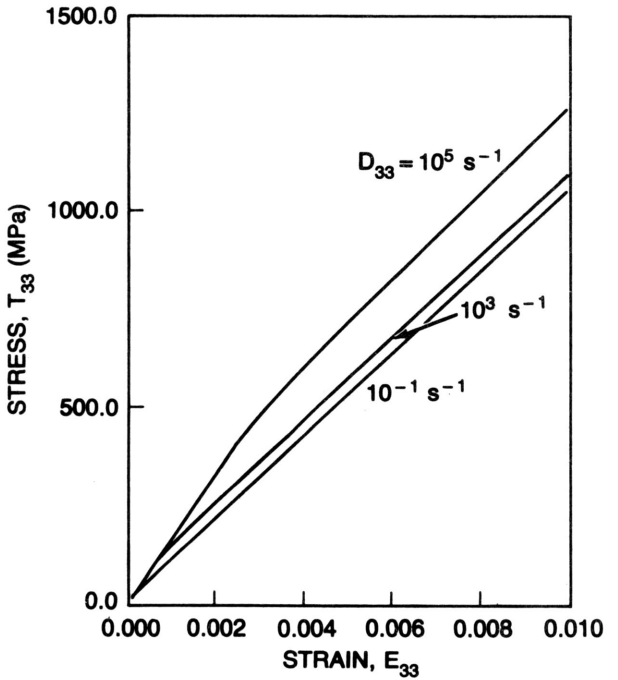

FIG. 5. Predicted stress-uniaxial strain response at different strain rates.

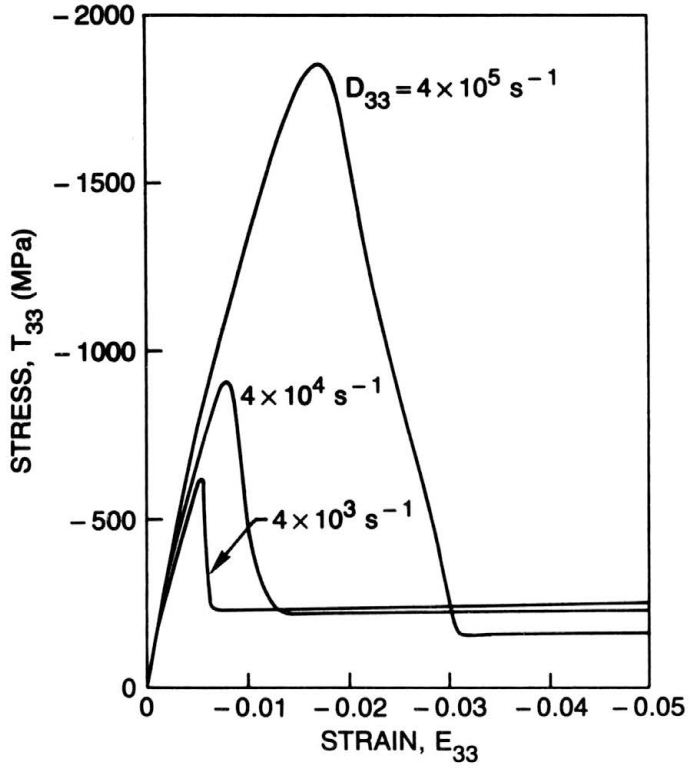

FIG. 6. Predicted stress-uniaxial strain response with damage at different strain rates.

In Fig. 6, which is also for uniaxial strain, the void volume fraction is allowed to increase. (The negative signs signify tensile stress and strain). These curves apart from showing the strong strain-rate hardening, illustrate the dramatic softening (relaxation of stress) effect, and its rate dependence, caused by the growing microvoid volume as the strain develops. The softening continues until the stress is reduced to the smaller of the void nucleation and void growth threshold stress values σ_N and σ_G. More discussion of these and other features of the damage behavior can be found in Ref. [22].

3. Simulation of plate impact spall fracture

3.1. Non-oblique plate impact

The constitutive theory presented in Sect. 2 can be used to simulate plate-impact spall fracture experiments where the spallation is ductile. The simplest and most frequently used plate-impact experimental configuration

utilizes flyer and target plates of the same material that have the same lateral dimensions (cf. Fig. 1). For a microsecond or so after impact the central portions of the plates experience uniaxial strain along the thickness direction in the form of longitudinal waves that propagate across the thickness and back, prior to arrival of release waves from the edges of the plates.

Detailed component expressions for the constitutive equations, and for the equations of motion, can be found in Ref. [23]. These equations are used in conjunction with the finite-difference wave propagation code (WONDY) to perform numerical simulations of plate-impact spall tests. Comparisons are made with experimental data for OFHC copper obtained from the literature. The experimental information includes: (i) distribution of the micro-damage across the target thickness, (ii) measurement of the stress-time profile at a gage embedded in a backup plate, and (iii) measurement of the velocity-time profile at the rear surface of the target.

For the first experimental simulation where a flyer plate 0.6 mm thick traveling at 160 m/s collides with a target plate 1.6 mm in thickness, the calculated compressive stress wave profiles that initially are propagating across the target are shown in Fig. 7. Considerable dispersion of the wave front is evident as the wave moves across the target, a manifestation of the viscous rate effect and nonlinear hardening of the material response. At 0.2 to 0.3 μs the leading edge of the elastic precursor wave begins to appear, followed by the slower moving viscoplastic wave front. At 0.3 μs the unloading edge of the compressive wave begins to develop, and at 0.4 μs the elastic-inelastic

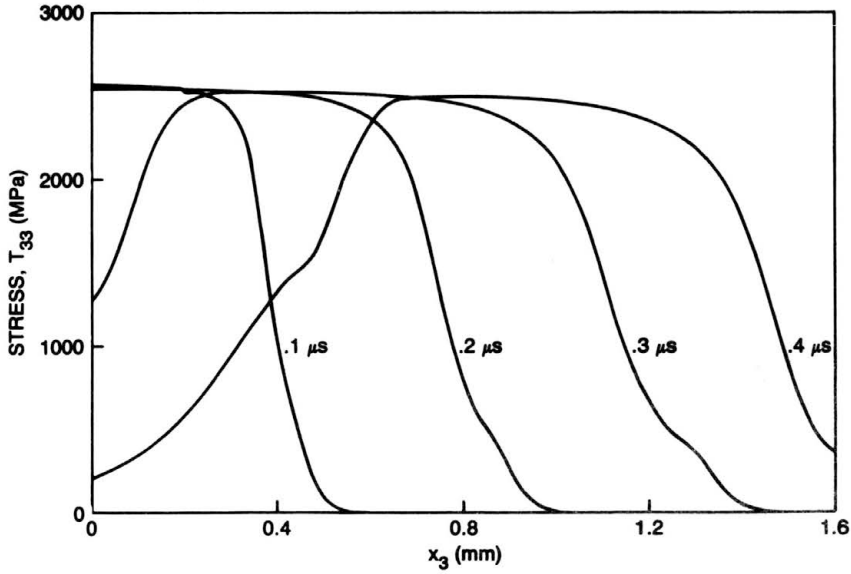

FIG. 7. Computed compressive stress wave profiles for 160 m/s impact.

two-part structure of the unloading wave front can clearly be seen. The tensile stress waves that are reflected in opposite directions from the rear surfaces of the plates superimpose to produce the material damage und ultimate spall facture of the target. Figure 8 shows the computed tensile stress distribution at different instants, demonstraing the progressive stress relaxation as the void volume fraction increases in the region of maximum tensile stress. The corresponding calculated distribution of the void volume fraction is shown by Fig. 9, which also shows the localization of the damage defining the approximate location of the spall fracture plane, as well as the correlation with measured porosity obtained from spalled copper plates [20].

In plate-impact testing stress can be measured indirectly by means of the arrangement shown schematically in Fig. 10, where a manganin wire gage is embedded in a low impedance buffer material, e.g., polymethalmethacrylate (PMMA), and placed behind the target. The measured [9] and calculated stress histories at the gage location (corresponding to the test simulation discussed above) appear in Fig. 11, showing qualitatively similar stress-time profiles, with close agreement between the time of arrival of the stress wave fronts. The second peak of the stress-time curve, referred to as the "spall signal", requires some explanation. As the initial compressive stress wave passes through the target, part of the wave is reflected back at the target-buffer interface as a rarefaction wave, possibly causing spall damage within the target. The remaining part continues on through the buffer resulting in the first compressive peak stress recorded by the stress gage. If damage takes place in the target,

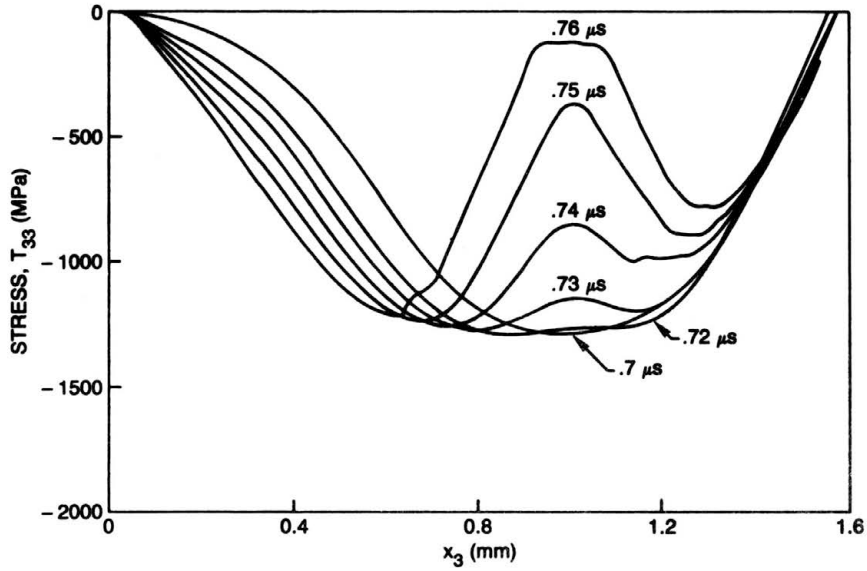

FIG. 8. Computed tensile wave profile illustrating the effect of damage accumulation (tensile stress is shown negative).

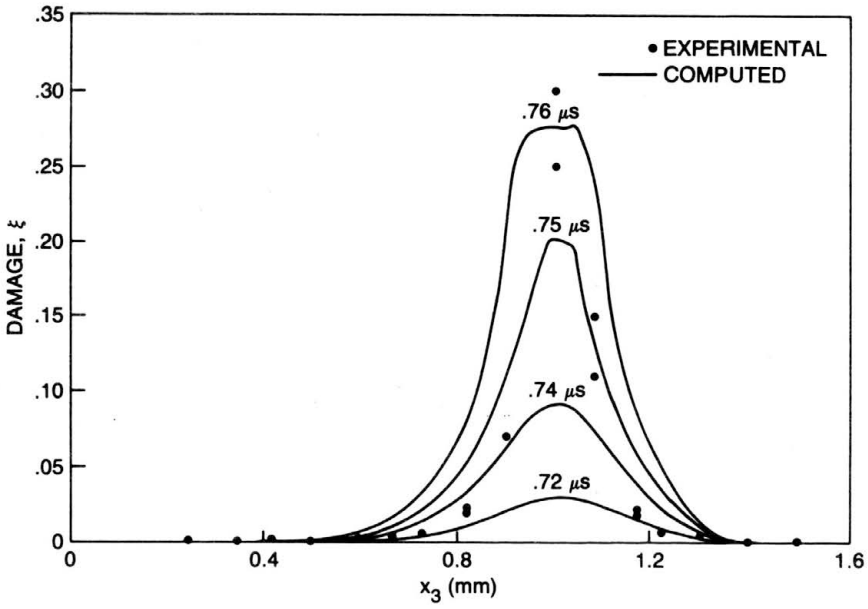

FIG. 9. Comparison of computed and measured void volume fraction across the thickness of the target plate.

a second compressive wave caused by recompression of the material adjacent to the damaged region as the tensile stress there is relaxed, travels to the right of the spall plane to the buffer surface. Part of this wave is reflected back into the target as a rarefaction wave, while the remaining part propagates through the backup buffer causing the second compressive peak stress at the stress gage, thus its identification as a spall signal. The amplitude of the second stress peak is related to the degree of the tensile stress relaxation in the target, and thus to the extent of the damage that has taken place.

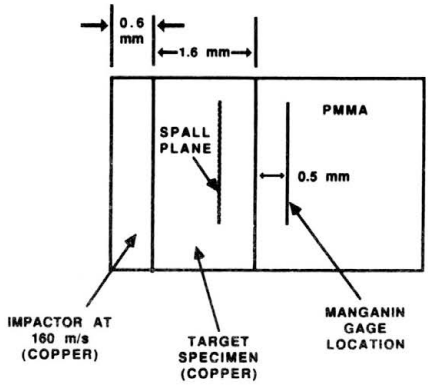

FIG. 10. Flyer-target-backup plate configuration showing embedded stress gage.

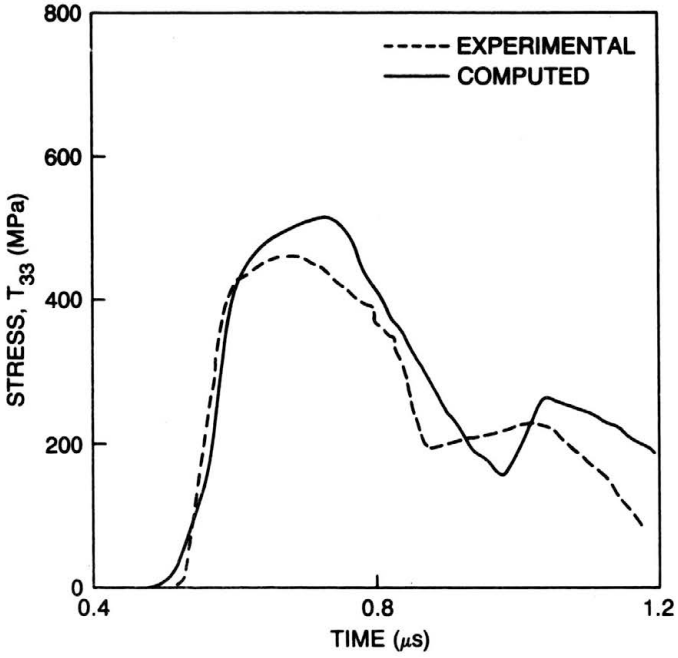

FIG. 11. Comparison of computed and measured stress histories at stress gage location for 160 m/s impact.

In a second experimental simulation the thickness of the plates are increased such that a 2 mm thick flyer impacts a 9 mm thick target at 185 m/s. The computed compressive wave profiles moving across the target are shown by Fig. 12. Because of greater thickness of target requiring a longer transit time, the characteristic features of the elastic-viscoplastic stress wave propagation are more fully developed. Clearly visible is the overall dispersion of the propagating wave, and the appearance of the elastic loading and unloading wave fronts that move further and further ahead of the slower viscoplastic wave. The localization and evolution of the damage within the target is shown by Fig. 13, where because of the greater target-flyer thickness ratio the potential location of the spall plane moves closer to the rear surface of the target. Figure 14 provides a comparison between the calculated rear surface velocity-time profile and measurements obtained by a velocity interferometer (VISAR) [41]. The calculated profile shows qualitative agreement with the measured profile, including the appearance of a spall signal, that is, of a second velocity peak due to the arrival of a second compressive wave that is associated with the appearance of a fracture surface in the target.

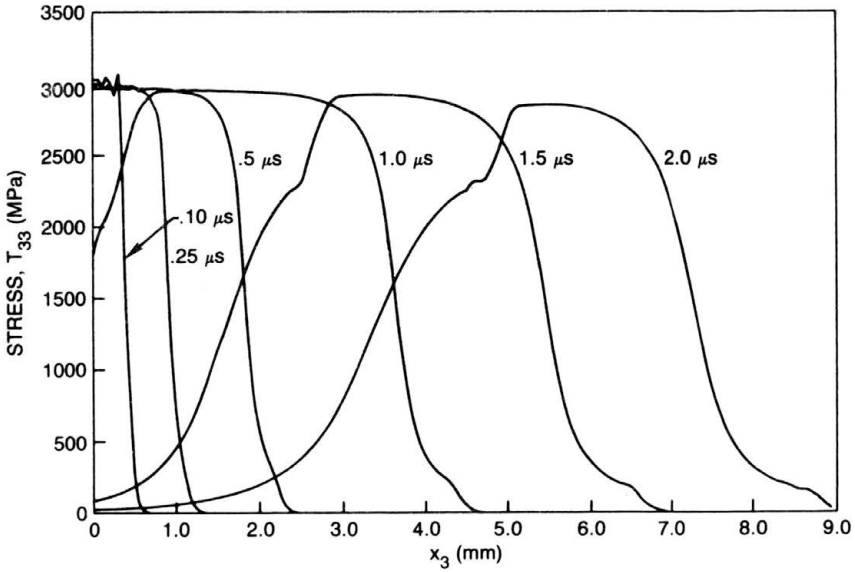

FIG. 12. Computed compressive stress wave profiles for 185 m/s impact.

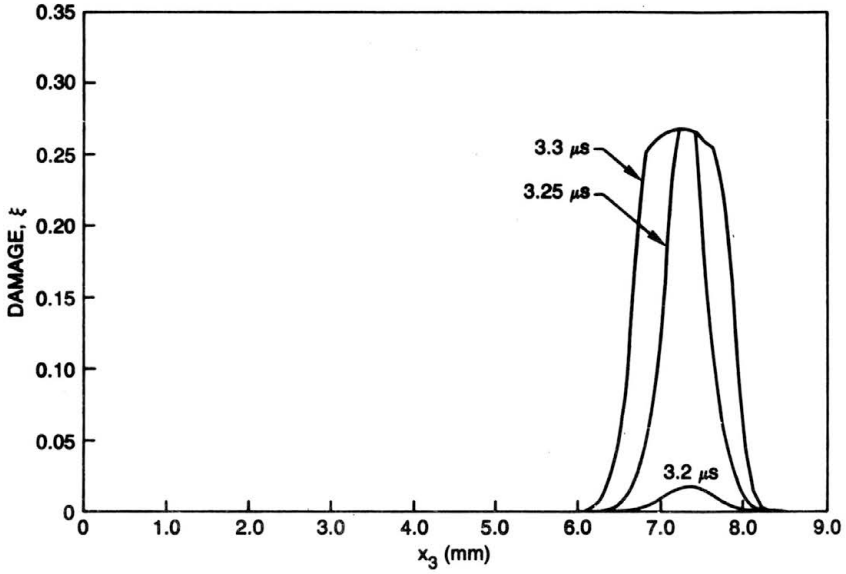

FIG. 13. Computed void volume fraction across the thickness of the target plate for 185 m/s impact.

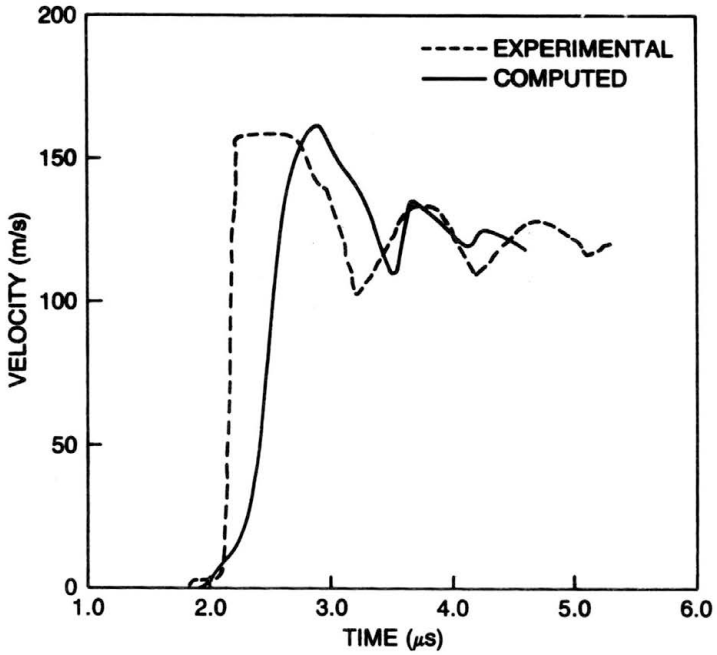

FIG. 14. Comparison of calculated and measured rear-surface velocity histories for 185 m/s impact.

3.2. Oblique plate impact

An oblique impact of plates can be realized when the flyer and target plates remain parallel but are inclined relative to the direction of the flyer velocity. The experimental configuration is shown schematically by Fig. 15.

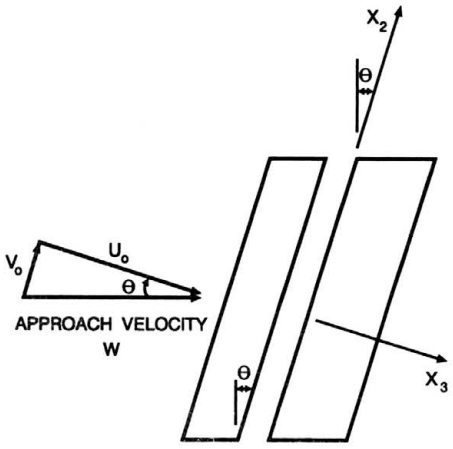

FIG. 15. Schematic of oblique flyer-target configuration.

This kind of plate arrangement imparts velocity components that are normal and transverse to the plane of impact, thereby creating shear stress as normal stress that vary along the direction of the plate thickness [42]. Thus far oblique plate impact experiments have been used principally for the study of plastic response of metals at strain-rates above those obtainable by the Hopkinson bar technique, with little, if any, work reported on its use for spall fracture studies under combined normal and shear stress waves [43—45].

The constitutive-damage model has been used to simulate low-angle oblique plate-impact experiments involving material damage and ductile spall fracture. With small angle of obliquity the mean stress that develops in the target will be approximately an order of magnitude greater than the shear stress, with the large tensile mean stress primarily responsible for the spall damage. The constitutive equations and the equations of motion, suitably specialized to the stress and rate of deformation conditions appropriate to the oblique impact test configuration, are used together with a modified version of the finite-difference computer code WONDY [46]. The analytical details of the constitutive modelization and analysis appear in Refs. [26, 28].

Oblique impact of plates produces elastic and plastic longitudinal and transverse waves. The elastic longitudinal wave propagating with wave speed C_{EL} is followed by the slower longitudinal plastic wave travelling at wave speed C_{PL}. These waves in turn are followed by slower elastic and plastic shear waves C_{ES} and C_{PS}, where $C_{EL} > C_{PL} > C_{ES} > C_{PS}$. The wave characteristics are shown schematically in Fig. 16, where the elastic and plastic longitudinal waves and the elastic shear wave are labeled by E, P and S, respectively. The plastic shear wave is not shown, and to further simplify the diagram the waves are drawn as if propagating at constant velocity, although in actuality they may not. The elastic wave speeds will change through change in value of the elastic constants when the stress thresholds for void volume increase are exceeded. The plastic wave speeds are affected by the strain hardening of the material and, conceivably, by damage accumulation as well. However, for purposes of illustration, one can construct the diagram with the wave speeds as constants without introducing serious qualitative error. The superposing of the oppositely directed elastic and plastic waves of rarefaction which occur at the times labeled as points (a) and (b) in Fig. 16, create the tensile mean stress causing material damage and spall fracture across a plane parallel to the faces of the plate. Point (d) corresponds to the time at which both reflected elastic and plastic rarefaction waves from the flyer free surface have crossed the flyer-target interface. Thereafter the normal stress across the plate reduces to zero, and from this time onward the shear induced by the interface friction between the plates stemming from the obliquity of the impact cannot develop, causing slip between the plates.

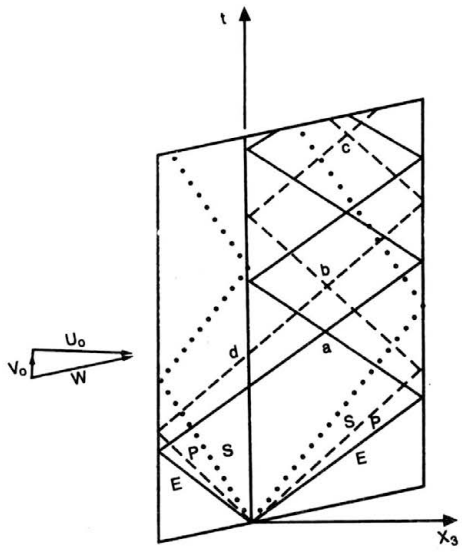

FIG. 16. Schematic distance-time plot showing wave paths.

The first test simulation has a 3 mm thick flyer impacting a 6 mm thick target with angle of obliquity $\theta = 26.6°$, which is the angle used in the experiments reported by KIM and CLIFTON [44]. The normal and tangential velocities of the oblique impact are $U_0 = 140$ m/s and $V_0 = 70$ m/s, respectively. The calculated normal compressive stress wave profiles for the T_{33} stress component appear in Fig. 17 showing the same features displayed in Fig. 7 for the nonoblique impact. This wave propagates prior to the onset of material damage, which takes place after the back surface reflection of the compressive stress wave. As may be seen from Fig. 18, the void damage process begins at 2.65 μs after impact, localized at the midplane of the target where the tensile mean stress attains peak value. Figure 19 shows the computed shear stress wave traveling at roughly one half the speed of the longitudinal wave. Between 0.25 μs and 1.0 μs there is relaxation of the shear stress at the front face of the target, and between 1.0 and 1.5 μs unloading of the stress wave begins. Thereafter the slip condition mentioned above begins at some instant between 1.5 and 2.0 μs, where the reduction of normal stress associated with arrival of the longitudinal rarefaction wave correspondingly reduces the friction induced shear stress to zero as shown by the stress profiles at 2.0 and 2.5 μs. The oscillations appearing at the left end of these profiles are numerical in origin.

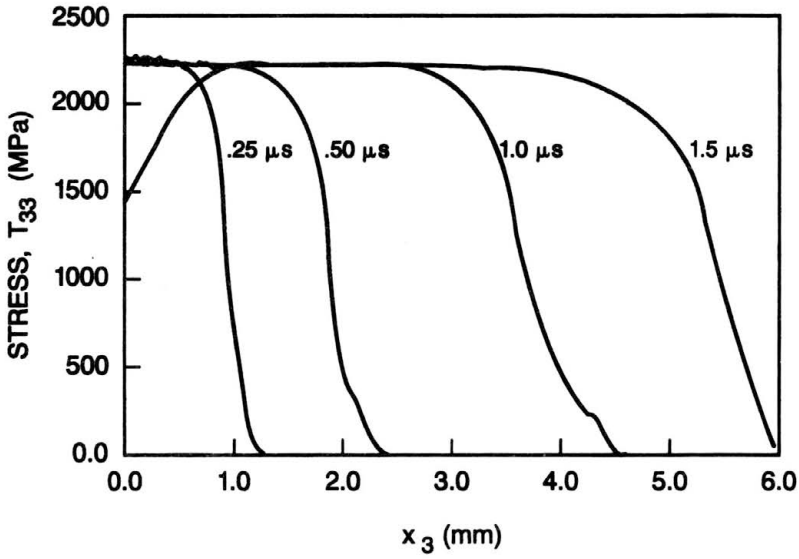

FIG. 17. Computed normal compressive stress wave profiles.

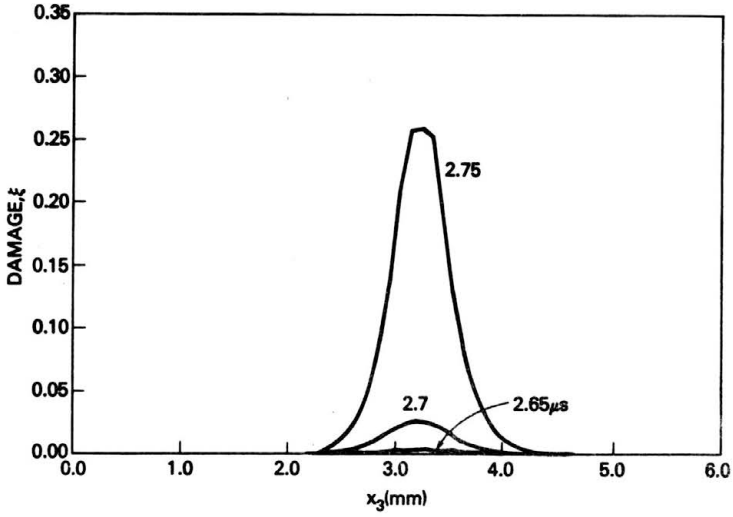

FIG. 18. Computed void volume fraction across the thickness of the target plate.

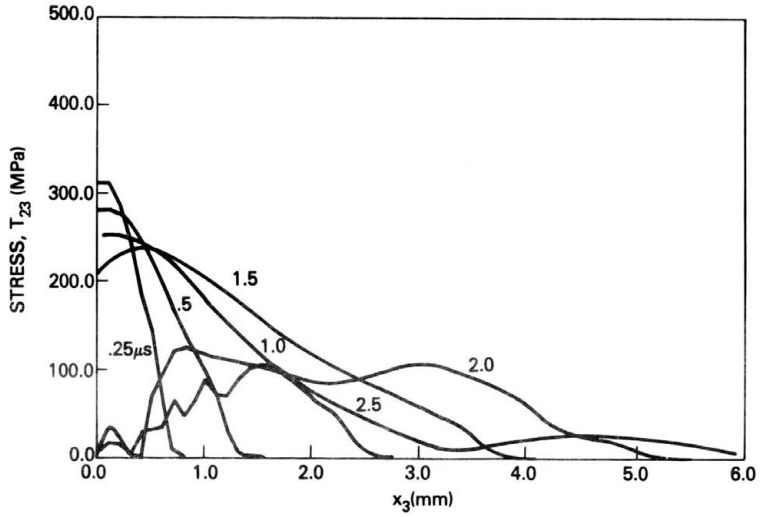

FIG 19. Computed shear stress wave profiles.

The predicted normal and transverse velocity histories at the rear surface of the target plate for this simulation are illustrated by Fig. 20. The normal velocity component which equals 140 m/s at the impact surface, shows little attenuation, rising to approximately 135 m/s at the rear surface. The characteristic spall signal is evident at 3.1 μs, just after the void volume fraction at the center of the plate approaches the spall condition at about 2.8 μs.

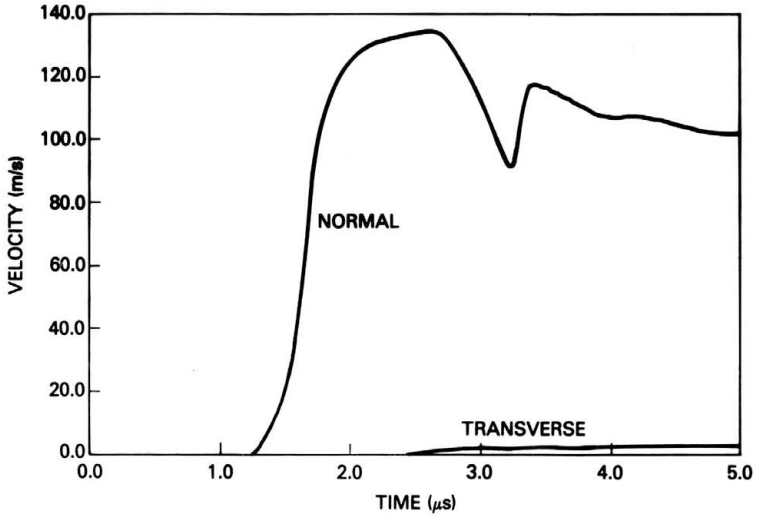

FIG. 20. Calculated rear surface velocities for $U_0 = 140$ m/s and $V_0 = 70$ m/s.

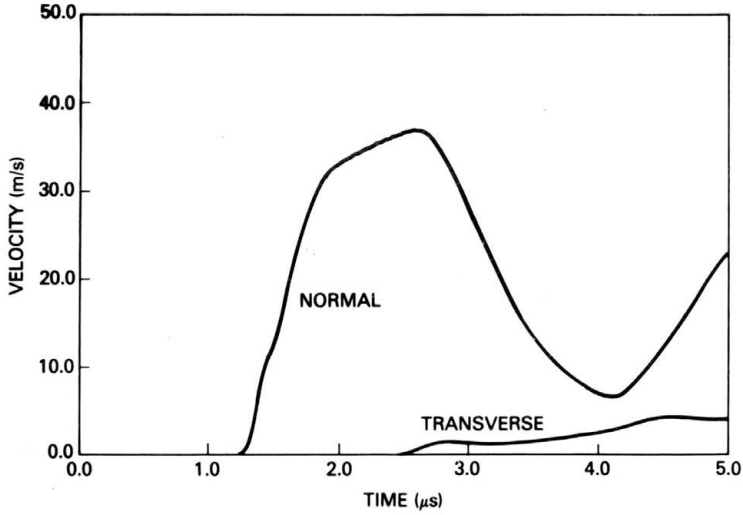

FIG. 21. Calculated rear surface velocities for $U_0 = 40$ m/s and $V_0 = 20$ m/s.

The decrease of the transverse velocity from 70 m/s at the impact surface to approximately 3 m/s at the rear surface can be explained as follows. In a second simulation the impact velocity components are reduced to $U_0 = 40$ m/s and $V_0 = 20$ m/s, insufficient to produce spallation. This may be seen by the corresponding rear surface velocity components shown by Fig. 21, where there is no spall signal in the normal velocity profile. The transverse

a)

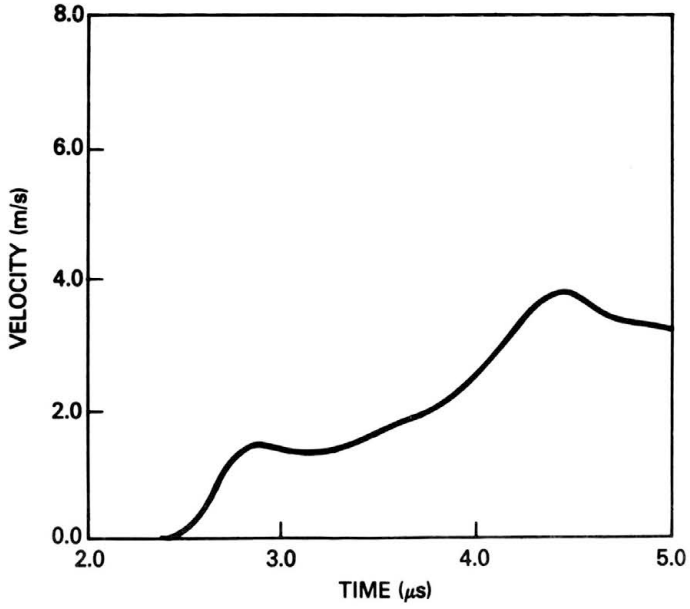

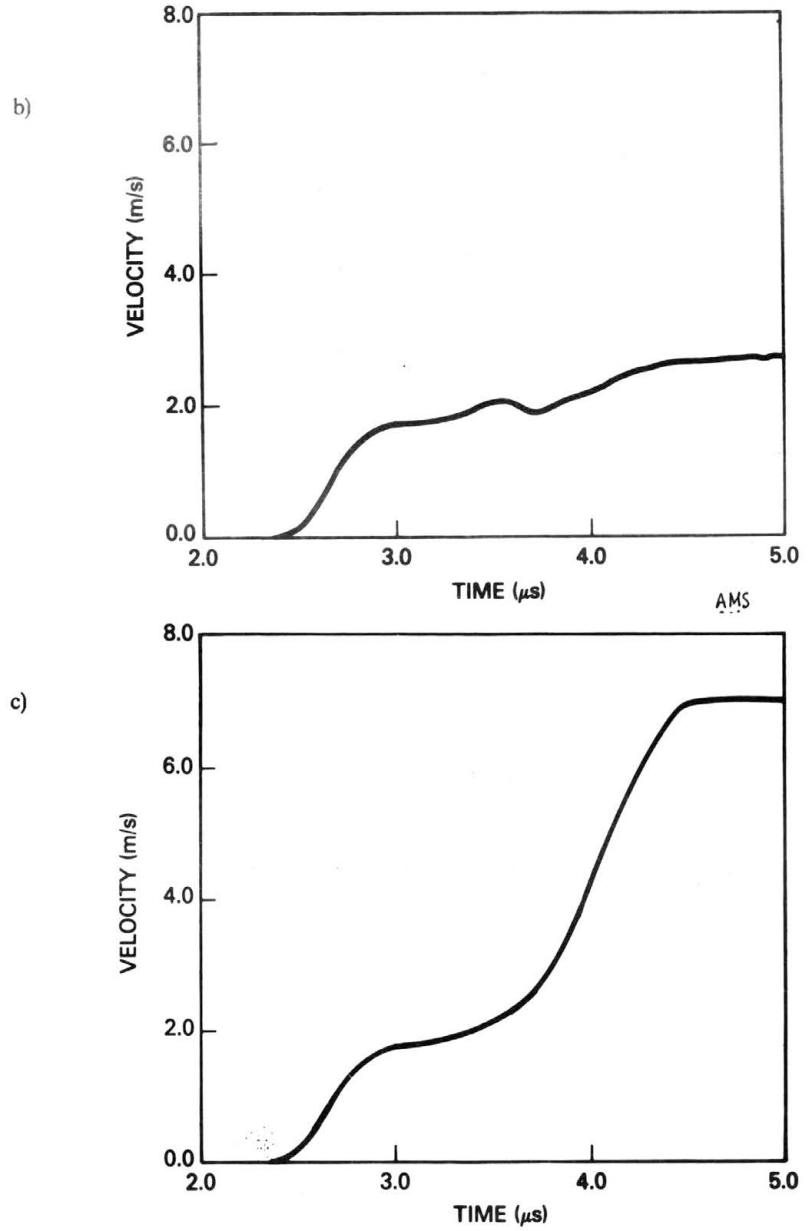

FIG. 22. Calculated rear surface velocities (a) $U_0 = 40$ m/s, $V_0 = 20$ m/s, (b) $U_0 = 140$ m/s, $V_0 = 70$ m/s, (c) $U_0 = 140$ m/s, $V_0 = 70$ m/s with damage suppressed.

velocity rises to approximately 4 m/s. More detail of the rear surface transverse velocity is shown in Figs. 22(a) to 22(c). Figure 22(a), which is for the smaller impact velocity (producing no spall damage) shows arrival of the elastic precursor shear wave at about 2.6 μs, followed by the slower plastic shear

wave. The decrease in transverse velocity, beginning at approximately 4.3 μs, reflects the propagation of the slip condition at the front face which occurred just prior to 2.0 μs. Figure 22(b) is an enlargement of the transverse velocity-time curve shown in Fig. 20, corresponding to the higher velocity of impact (producing spall damage). The leading elastic shear wave is followed by a plateau. However there is no substantial increase in the transverse velocity associated with arrival of the plastic shear wave. It seems plausible, therefore, that the lack of a substantial plastic wave can be attributed to the damage accumulation which would prevent the plastic shear from being transmitted after the elastic shear had propagated through the material prior to the onset of microvoid growth. This appears to be confirmed by the rear surface transverse velocity history shown in Fig. 22(c). The physical conditions for Fig. 22(c) are the same as for 22(b) (high impact velocity and spall damage), with the exception that the generation of damage following the impact has been suppressed. Without growth of the microvoid volume the transverse velocity profile of Fig. 22(c) now shows arrival of the elastic shear wave followed by a plastic wave front, similar overall in form to the velocity profile of Fig. 22(a) for which there was no damage because of the low velocity of impact.

On the basis of these results, it appears that for oblique-impact experiments the form of the shear wave signal appearing in the target rear surface transverse velocity history can serve as an additional indicator of the inelastic-damaged response of the target material, similar to the spall signal that appears in the normal velocity profile.

3.3. Non-oblique impact of circular plates with unequal diameters

The third plate-impact experimental configuration studied employs thin circular plates that have different diameters (cf. Fig. 23). An edge effect is introduced because of the diameter difference. This causes radially directed waves as well as waves that propagate across the target thickness, (cf. Fig. 24),

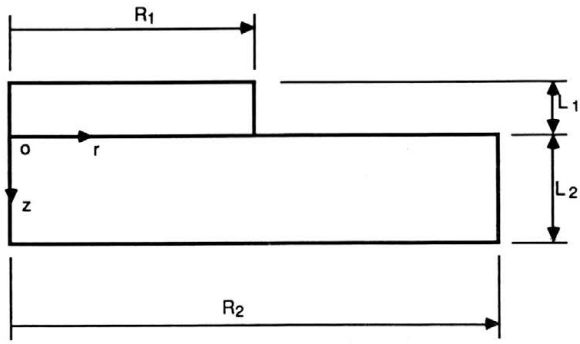

FIG. 23. Circular flyer and target plate dimensions.

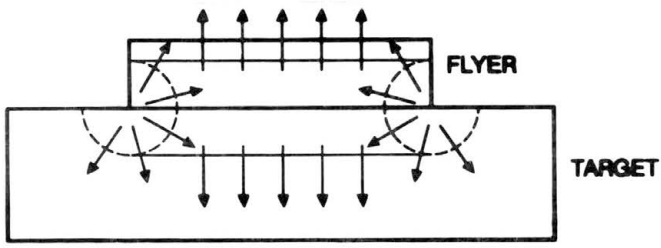

FIG. 24. Impact of the circular flyer with a larger diameter target.

carrying three normal components and one radially directed shear component for the stress and for the strain. The plate dimensions for the flyer are radius $R_1 = 20\,\text{mm}$, thickness $L_1 = 3\,\text{mm}$, and for the target radius $R_2 = 40\,\text{mm}$ and thickness $L_2 = 6\,\text{mm}$. The numerical simulations were carried out for a total time of $5\,\mu\text{s}$ after impact, sufficient for several wave propagations across the target thickness. Because of the smaller diameter of the flyer, spall initiates only over the central region of the target. The post-spall behavior of the partially fractured target plate was modeled by carrying the numerical calculations to a total time of $50\,\mu\text{s}$. The calculations required use of the transient finite-element computer code PRONTO [47] and were carried out on a Cray X–MP computer. A detailed presentation and discussion of the equations of motion, the constitutive rate equations, the boundary and initial conditions for the given plate geometries, as well as the numerical methods employed are given in Ref. [29].

3.3.1. Effect of impact velocity. Several simulations were performed over a range of impact velocities from which it was possible to estimate a damage threshold velocity of approximately 50 m/s, in agreement with previous experimental and computational results for copper plates having the same flyer-thickness ratio [24, 28]. It is also noted that for these computations there is no actual separation of the material in the sense that the constitutive model does not issue instructions for the severing of the element grid lines across the potential spall plane. Numerically the material continues to be modeled as a continuum in which extensive material damage takes place across the region of the plate cross-section that includes this plane, appearing as excessive elongation of the mesh elements. This is illustrated by Figs. 25(a)—25(c), where (a), (b), (c) correspond to impact velocities of 100, 200 and 350 m/s, respectively. These figures represent the plate configuration at 5 μs after impact. (For illustrative purposes the computed deformations shown in the figures have been magnified by a factor of three). The corresponding contours of the void volume fraction across the plate thickness are shown by Fig. 26. Both figures reveal the pronounced effect of increasing the flyer impact velocity. At 100 m/s the void volume of the target along midplane shows increase,

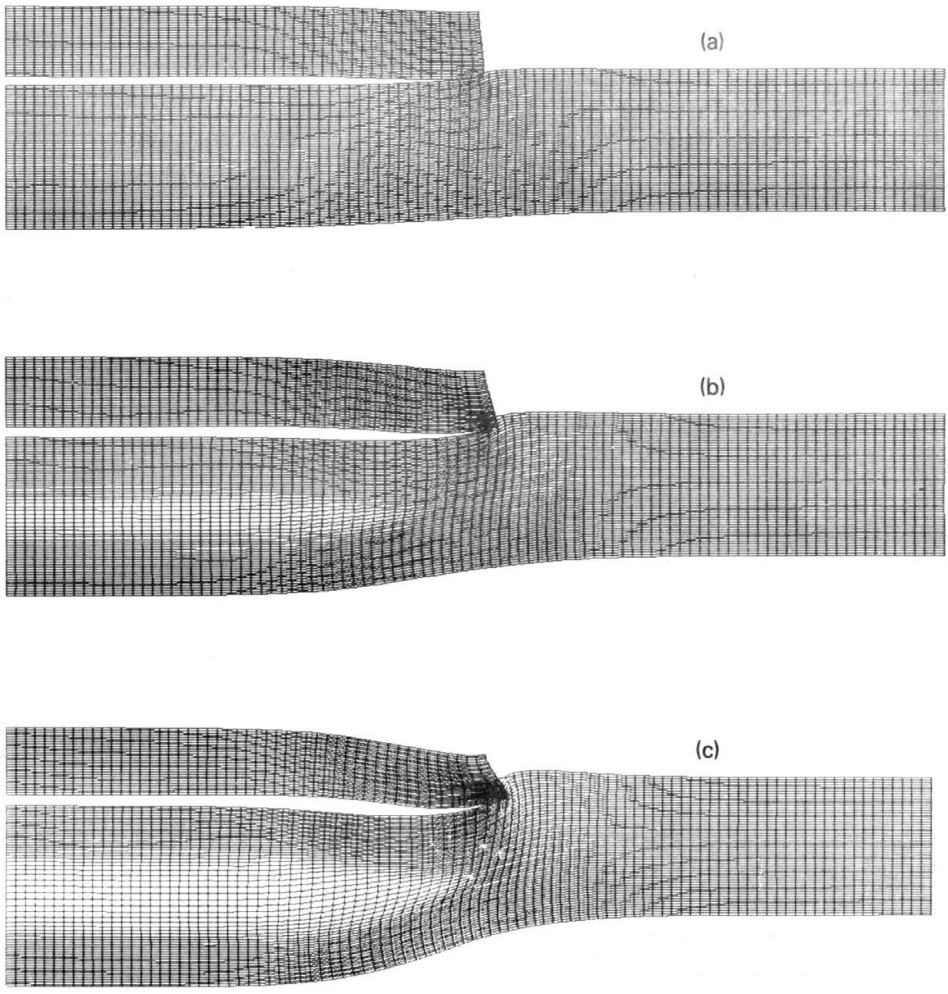

FIG. 25. Deformed geometry at 5 μs post-impact for impact velocity at (a) 100 m/s, (b) 200 m/s, (c) 350 m/s.

although well below the critical value at 0.32. Correspondingly, material softening accompanies the growth with elongation of the mesh elements across the midplane. This becomes more evident at 200 m/s impact velocity where the void volume approaches 0.32 over the mid-plane region implying spall fracture across the midplane. At 350 m/s impact the rear spalled section of the target has sufficient momentum to cause further widening of the opening in the plate.

With the impact velocity at 350 m/s Fig. 27(a) displays the time variation of the location of the contour for the T_{zz} normal stress component at 6000 MPa compression. From 1.0 to 1.5 μs the reflected tensile stress wave from the back surface of the flyer travels forward causing forward shift of the location of the

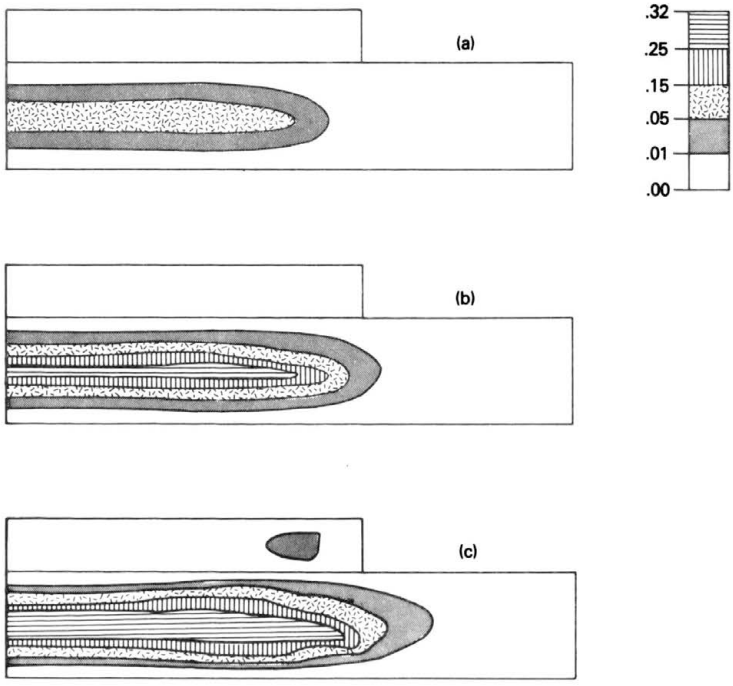

FIG. 26. Contours for void volume fraction for impact velocity at (a) 100 m/s, (b) 200 m/s, (c) 350 m/s.

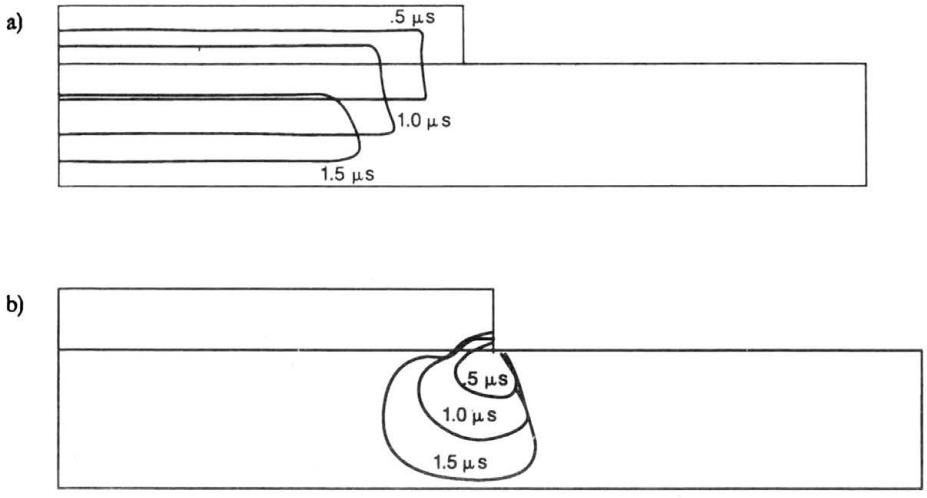

FIG. 27. Time variation of stress contours after impact at 350 m/s velocity (a) $T_{zz} = 6000$ MPa, (b) $T_{rz} = 150$ MPa.

compressive stress contour. Simultaneously the inward movement of the vertical edge of the contour reflects the interaction with the non-planar radial wave from the circumferential edge of the flyer, reducing the diameter of the region of the target experiencing the very high mean stress. This would seem to indicate why the diameter of the spalled surface initially is smaller than the diameter of the flyer. However, as Fig. 25 graphically illustrates, as the velocity of impact increases, the correspondingly larger momentum of the spalled section of the target causes the diameter of the area of separation to widen.

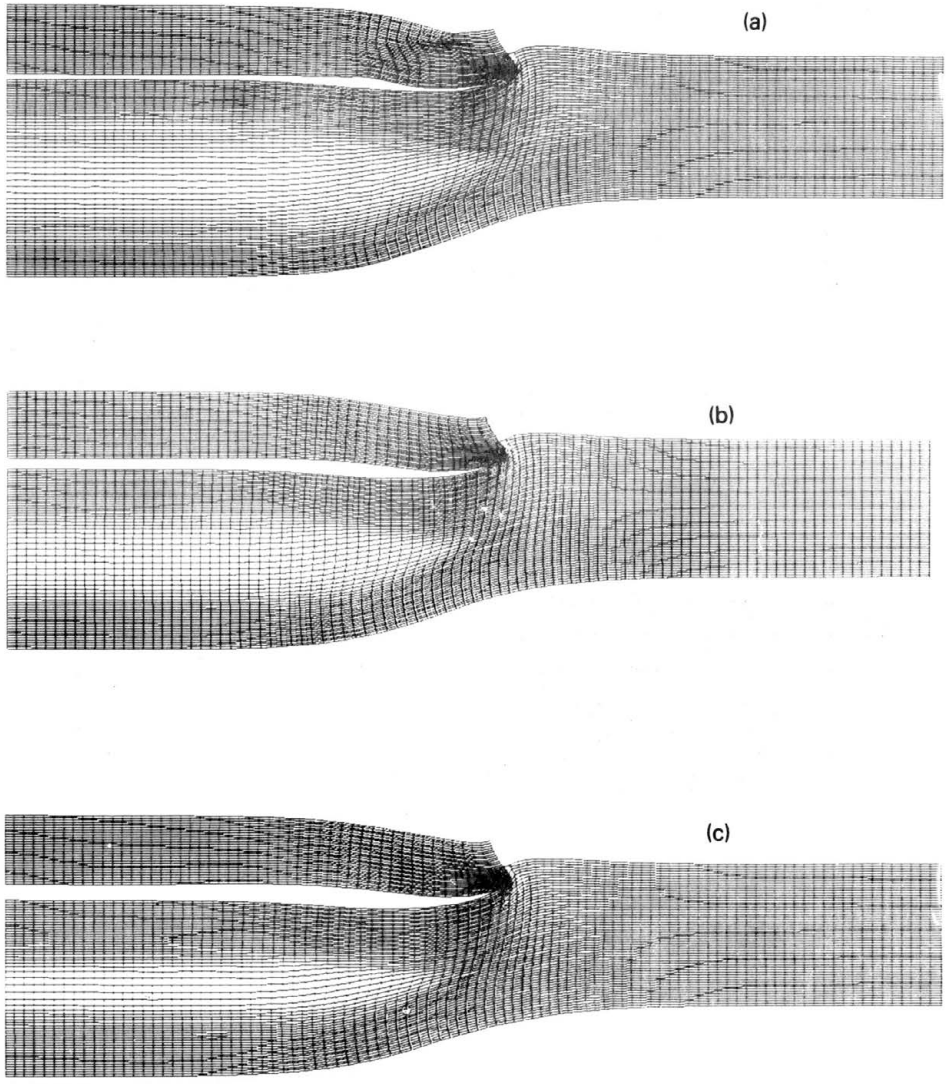

FIG. 28. Deformed geometry at 5 μs post-impact for microviscosity parameter η at (a) 10P, (b) 120P, (c) 500P.

Figure 27(b) provides a similar plot for contours of the shear stress T_{rz} at 150 MPa at 0.5, 1.0 and 1.5 μs following impact at 350 m/s. The stress contours reflect the propagation of the non-planar shear wave from the edge of the flyer traveling radially in, toward the center and across the target thickness.

3.3.2. Variation of the microviscosity material parameter. The results of having varied several of the material parameter values related to the microvoid growth [25, 37] has shown that the microviscosity η has a large influence on the behavior of the damaged material. It is apparent from Eq. (2.27) that larger values for the microviscosity has the effect of reducing the rate of void growth, while Eq. (2.29) indicates an associated hardening effect as the void volume fraction is reduced. With the flyer impact velocity at 350 m/s several numerical simulations were performed with the microvoid viscosity parameter η assigned values of 10P, 120P and 500P. The plate configurations and the void volume fraction contours at 5 μs post-impact are shown by Figs. 28 and 29, respectively, illustrating the controlling influence of this material parameter on the development of void growth and ductile material damage. As the microviscosity increases in value, the extent of damage that can develop in the material

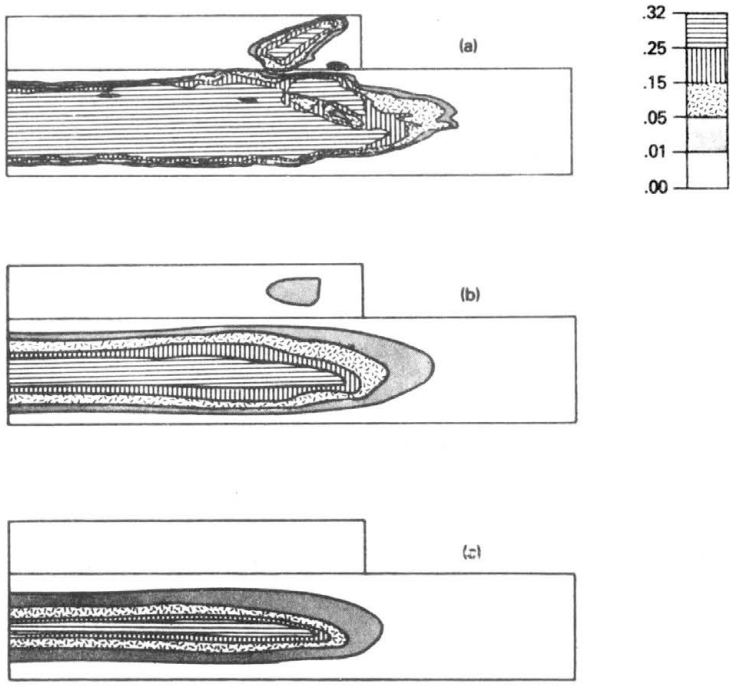

FIG. 29. Contours for void volume fraction for microviscosity parameter η at (a) 10P, (b) 120P, (c) 500P.

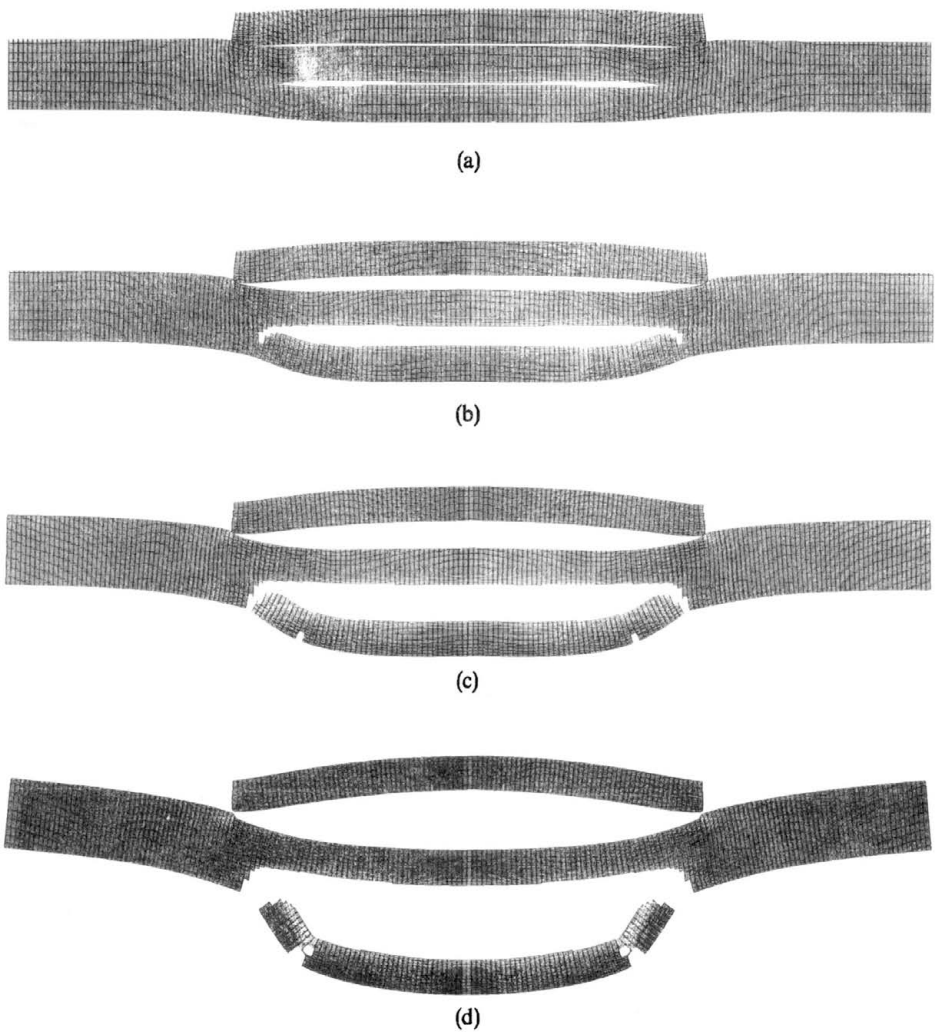

FIG. 30. Deformed geometry for a 3.0 mm flyer with 350 m/s impact velocity at (a) 5 μs, (b) 15 μs, (c) 25 μs, (d) 50 μs.

after 5 μs is reduced considerably, while the material, which has correspondingly smaller void volume, experiences greater strain hardening.

3.3.3. Post-spall behavior. The deformation of the plates at 5, 15, 25 and 50 μs after impact by the flyer traveling at 350 m/s are shown by Figs. 30(a)—30(d). In these figures the deformation has not been magnified as in Figs. 25 and 28. Also the element deletion capability available in the PRONTO computer code was

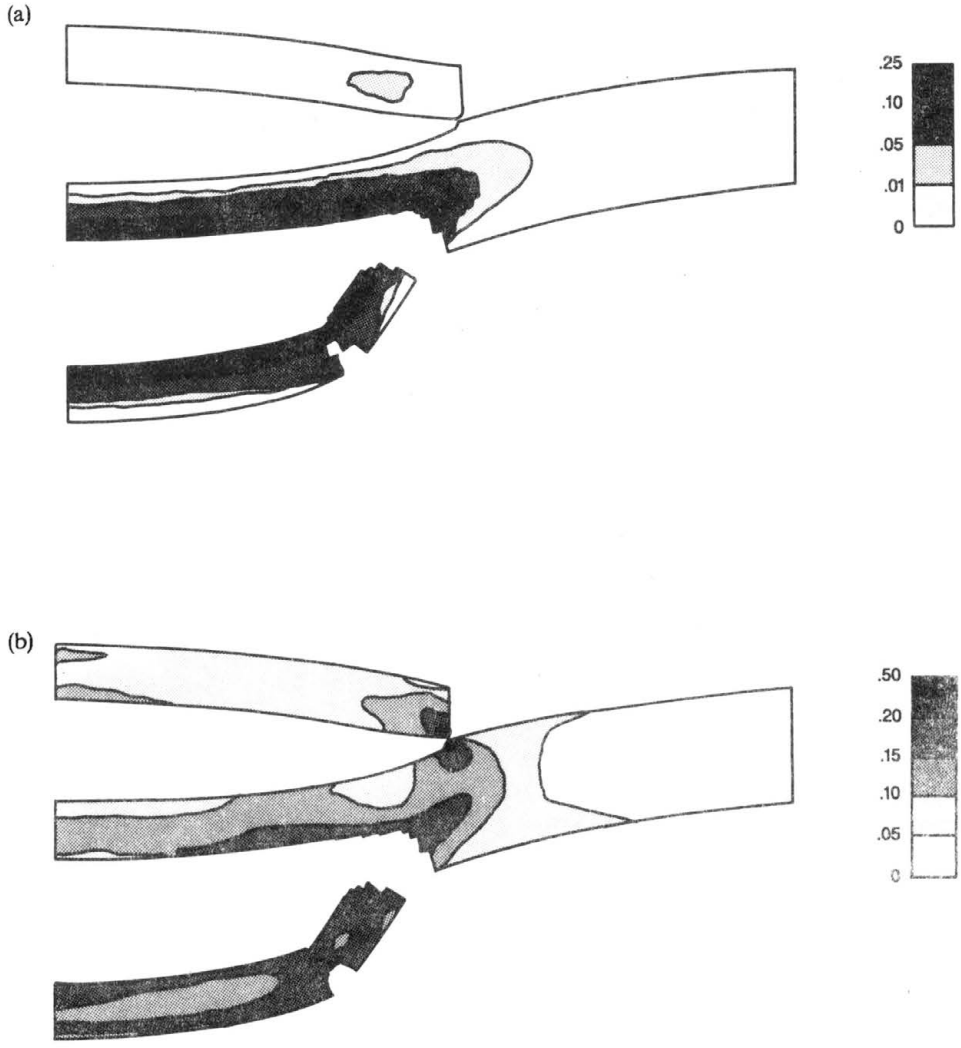

FIG. 31.(a). Accumulated plastic strain at 50 μs. (b). Void volume fraction at 50 μs.

utilized, where upon reaching a prescribed void volume fraction the stresses in the finite element are set to zero over several time steps and the element is delated from further calculations.

At 5 μs spall has developed along the mid-plane of the target, withthe rear portion of the spalled segment moving out and away from the remainder of the plate with momentum sufficient to cause it to continue its outward motion. This leads to fracture at the edges of the spall seen at 15 μs. The progressive deletion of elements along the edge of the spall simulates a shearing of the spalled material away from the remainder of the target.

Actually it is the large tensile stress that develops as the deformation localizes to a row of elements across the spall that causes the increase in void volume fraction and subsequent deletion, with little increase in void volume adjacent to the detached edges. By 25 μs the spalled segment has detached and has developed some additional fractures near the detached edges along the outer highly curved tensile edge. At 50 μs these edge fractures have advanced almost entirely across the fragmet. Calculations at later times show only minor changes from the configuration at 50 μs, indicating that no further fracturing of the segment is to be expected. Figure 31(a) displays the void volume distribution at 50 μs where, as expected, the highest values are adjacent to the spall plane. The equivalent plastic strain distribution across the plates is shown in Fig. 31(b). Here the regions of highest plastic strain are those in which the edge effects are present due to the larger shear deformation that occurs. In particular, the outer edge of the flyer along the flyer-target interface and the edge of the spall, are regions of high shear deformation that is reflected in the higher values of the equivalent plastic strain.

3.3.4. Change of the plate thickness ratio. In the calculations thus far the flyer plate thickness was one-half the thickness of the target. For this thickness ratio the spall plane is located at the mid-plane of the target. In the next plate impact test simulation the flyer thickness is reduced to one-quarter the target thickness, that is, $L_1 = 1.5$ mm with $L_2 = 6.00$ mm. With the flyer impact velocity at 350 m/s, Figs. 32(a)–32(d) show the plate configurations at 5, 15, 25 and 50 μs after impact. As to be expected, because of the thinner flyer the reflected tensile stress wave from the rear surface of the flyer enters the target sooner, thereby superimposing with the reflecting tensile stress wave from the rear surface of the target at a location closer to this surface. The spall plane is now located further back at three fourths the distance to the rear surface. The comparatively thinner rear segment of the spalled plate, having less momentum than the spalled segment of the previous simulation, is insufficient to cause fragmentation.

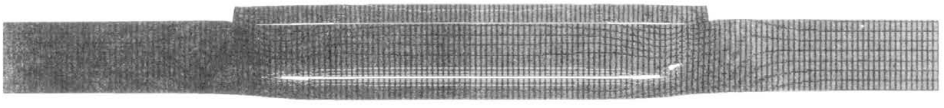

(a)

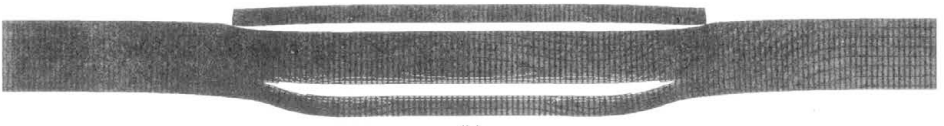

(b)

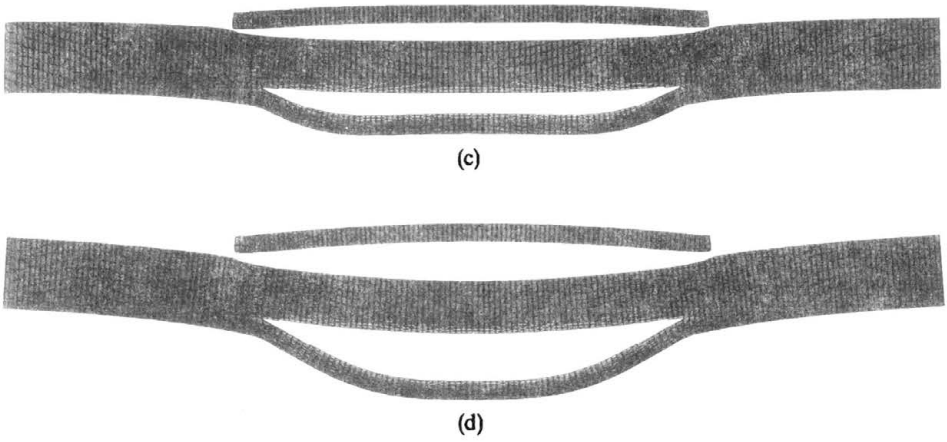

FIG. 32. Deformed geometry for a 1.5 mm flyer with 350 m/s impact velocity at (a) 5 μs, (b) 15 μs, (c) 25 μs, (d) 50 μs.

Acknowledgments

The authors would like to acknowledge the interest and support for the spall fracture work extended by Dr. Phillip RANDLES and by Dr. Robert BADALIANCE, Branch Head, of the Mechanics of Materials Branch at the Naval Research Laboratory, and by the ASEE-NAVY Summer Faculty Research Program.

References

1. D. R. CURRAN, *Dynamic fracture*, in: Impact Dynamics, 333—366, J. ZUKAS *et al.* [eds.], J. Wiley, New York 1982
2. J.S. RINEHART and J. PEARSON, *Behavior of metals under impulsive loads*, American Society for Metals, 1954, Dover Pub., New York 1965.
3. J. GILATH and J. ELIEZER, *Pulsed laser induced spall, a new method to study dynamic properties*, Advances in Plasticity, 393—396, 1989, A.H. KHAN and M. TOKUDA [eds.], Pergamon Press, Oxford 1989.
4. B.M. BUTCHER, L.M. BARKER, D.E. MUNSON and C.D. LUNDERGAN, *Influence of stress history on time-dependent spall in metals*, AIAA J., 2, 977—990, 1964.
5. F.R. TULER and B.M. BUTCHER, *A criterion for the time dependence of dynamic fracture*, Int. J. Fract., **4**, 431—437, 1968.
6. J.J. GILLMAN and F.R. TULER, *Dynamic fracture by spallation in metals*, Int. J. Fract., **6**, 169—182, 1970.
7. T.W. BARBEE, L. SEAMAN, R. CREWDSON and D. CURRAN, *Dynamic fracture criteria for ductile and brittle metals*, J. Mater., **7**, 393—401, 1972.

8. L. SEAMAN, D.A. SHOCKEY and D.R. CURRAN, *The growth law for crack propagation under shock conditions*, in: Dynamic Crack Propagation, 629—647, G.H. SIH [ed.], Noordhoff, Leyden 1973.
9. L. SEAMAN, D.R. CURRAN and D.A. SHOCKEY, *Computational models for ductile and brittle fracture*, J.Appl.Phys., **47**, 4814—4826, 1976.
10. D.R. CURRAN, L. SEAMAN and D.A. SHOCKEY, *Dynamic failure in solids*, Physics Today, 46—55, January 1977.
11. D.A. SHOCKEY, L. SEAMAN and D.R. CURRAN, *Microfailure models and their application to nonlinear dynamic fracture problems*, in: Nonlinear and Dynamic Fracture Mechanics, ASME, Appl. Mech.Div., **35**, 79—104, 1979.
12. L. SEAMAN, D.R. CURRAN and W.J. MURRI, *A continuum model for dynamic tensile microfracture and fragmentation*, J.Appl.Mech., **52**, 593—600, 1985.
13. D.A. SHOCKEY, L. SEAMAN and D.R. CURRAN, *The micro-statistical fracture mechanics approach to dynamic fracture problems*, Int. J.Fracture, **27**, 1985.
14. L. DAVISON and A.L. STEVENS, *Continuum measures of spall damage*, J.Appl.Phys., **43**, 988—944, 1972.
15. L. DAVISON and A.L. STEVENS, *Thermomechanical constitution of spalling elastic bodies*, J.Appl.Phys., **44**, 1973.
16. L. DAVISON, A.L. STEVENS and M.E. KIPP, *Theory of spall damage accumulation in ductile metals*, J.Mech.Phys.Solids, **25**, 11—28, 1977.
17. D.E. GRADY, *Local inertial effects in dynamic fragmentation*, J.Appl.Phys., **53**, 322—325, 1982.
18. D.E. GRADY, *The spall strength of condensed matter*, J.Mech.Phys.Solids, **36**, 353—384, 1988.
19. M.A. MEYERS and C.T. AIMONE, *Dynamic fracture (spalling) of metals*, Prog. in Mater. Sci., **28**, 1—96, 1983.
20. D.R. CURRAN, L. SEAMAN and D.A. SHOCKEY, *Dynamic failure of solids*, Phys. Reports, **147**, 253—388, 1987.
21. P. PERZYNA, *Internal state variable description of dynamic fracture of ductile solids*, Int.J.Solids Struct., **22**, 797—818, 1986.
22. J.A. NEMES, J. EFTIS and P.W. RANDLES, *Viscoplastic constitutive modeling of high strain-rate deformation, material damage, and spall fracture*, Trans. ASME, J.Appl.Mech., **57**, 282—291, 1990.
23. J. EFTIS, J.A. NEMES and P.W. RANDLES, *Viscoplastic analysis of plate-impact spallation*, Int. J.Plasticity, **7**, 15—39, 1991.
24. J.A. NEMES and J. EFTIS, *Use of viscoplastic constitutive theory for simulating spallation thresholds*, in: Shock Waves in Condensed Matter, 369—372, 1989, S.C. SCHMIDT *et al.* [eds.], Elsevier Sci. Pub., Amsterdam 1990.
25. J. EFTIS and J.A. NEMES, *Evolution equation for the void volume growth rate in viscoplastic--damage constitutive model*, Int. J.Plasticity, **7**, 275—293, 1991.
26. J.A. NEMES and J. EFTIS, *Low-angle oblique impact spall fracture using viscoplastic constitutive theory*, in: Advances in Constitutive Laws for Engineering Materials, vol. II, 633—639, Int.Acad.Pub., Beijing 1989.
27. J.A. NEMES and J. EFTIS, *Several features of a viscoplastic study of plate-impact spallation with multidimensional strain*, Computers and Structures, **38**, 317—328, 1991.
28. J.A. NEMES and J. EFTIS, *Pressure-shear waves and spall fracture described by a viscoplastic--damage constitutive model* (forthcoming in Int.J.Plasticity).
29. J. EFTIS and J.A. NEMES, *Modeling of impact-induced spall fracture and post-spall behavior of a circular plate* (forthcoming in Int.J.Fracture).
30. J.H. MACKENZIE, *The elastic constants of a solid containing spherical holes*, Proc.Phys.Soc., **63B**, 2—11, 1950.

31. P. PERZYNA, *The constitutive equations for rate sensitive plastic materials*, Quart. Appl.Math., **20**, 321—332, 1963.
32. S. SHIMA and M. OYANE, *Plasticity theory for porous solids*, Int.J.Mech.Sci., **18**, 285—291, 1976.
33. J.W. HANCOCK, *Plasticity of porous metals*, in: Yield, Flow and Fracture of Polycrystals, 69—79, T.N. BAKER [ed.], Applied Sci. Pub., Essex 1983.
34. S.M. DORAIVELU, H.L. GEGEL, J.S. GUNASEKERA, J.C. MALAS, J.J. MORGAN and J.S. THOMAS, *A new yield function for compressible P/M materials*, Int. J.Mech.Sci., **26**, 527—535, 1984.
35. M.M. CARROLL and A.C. HOLT, *Static and dynamic pore-collapse relations for ductile solids*, J.Appl.Phys., **43**, 1626—1636, 1972.
36. J.N. JOHNSON, *Dynamic fracture and spallation in ductile solids*, J.Appl.Phys., **53**, 2812—2825, 1981.
37. J.A. NEMES, *A viscoplastic description of high strain-rate deformation, material damage and spall fracture*, DSc Dissertation, G. Washington Univ., Washington 1989.
38. T. NICHOLAS, *Material behavior at high strain rates*, in: Impact Dynamics, 277—331, J. ZUKAS *et al.* [eds.], J. Wiley and Sons, New York 1982.
39. A.R. DOWLING, J. HARDING and J. CAMPBELL, *The dynamic punching of metals*, J.Inst. Metals, **98**, 215—224, 1970.
40. C.H. KARNES, *The plate impact configuration for determining mechanical properties of materials at high strain rates*, in: Mechanical Properties of Materials under Dynamics Loads, U.S. LINDHOLM [ed.], Springer–Verlag, New York 1968.
41. A.M. RAJENDRAN, D.J. GROVE and S.J. BLESS, *A new yield function based dynamic failure model*, in: Shock Waves in Condensed Matter, 1987, S. SCHMIDT *et al.* [eds.], Elsevier Sci. Pub., Amsterdam 1988.
42. A.S. ABOU-SAYED, R.J. CLIFTON and L. HERMANN, *The oblique-plate impact experiment*, Exp. Mech., **16**, 127—133, 1976.
43. A.S. ABOU-SAYED and R.J. CLIFTON, *Analysis of combined pressure-shear waves in an elastic/viscoplastic material*, J.Appl.Mech., **44**, 70—84, 1977.
44. K.S. KIM and R.J. CLIFTON, *Pressure-shear impact of 6061–76 aluminium*, J.Appl.Mech., **47**, 11—16, 1980.
45. R.W. KLOPP, R.J. CLIFTON and T.G. SHAWKI, *Pressure-shear impact and the dynamic viscoplastic response of metals*, Mech. Materials, **4**, 375—385, 1985.
46. M.E. KIPP and R.J. LAWRENCE, *WONDY-V, A one-dimensional finite difference wave propagation code*, SAND 81—0930, Sandia Laboratories, Albuquerque 1982.
47. L.M. TAYLOR and D.P. FLANAGAN, *PRONTO 2D, A two-dimensional transient solid dynamics program*, SAND86—0594, Sandia National Laboratories, Albuquerque 1987.
48. J.H. SMITH, *Three low pressure spall thresholds in copper*, in: Dynamic Behavior of Materials, 264—282, American Society for Testing Materials, Philadelphia 1963.

DEPARTMENT OF CIVIL, MECHANICAL AND ENVIRONMENTAL ENGINEERING
THE GEORGE WASHINGTON UNIVERSITY, WASHINGTON
and
MECHANICS OF MATERIALS BRANCH, MATERIALS SCIENCE AND TECHNOLOGY DIVISION
NAVAL RESEARCH LABORATORY, WASHINGTON, USA.

Received March 15, 1991.